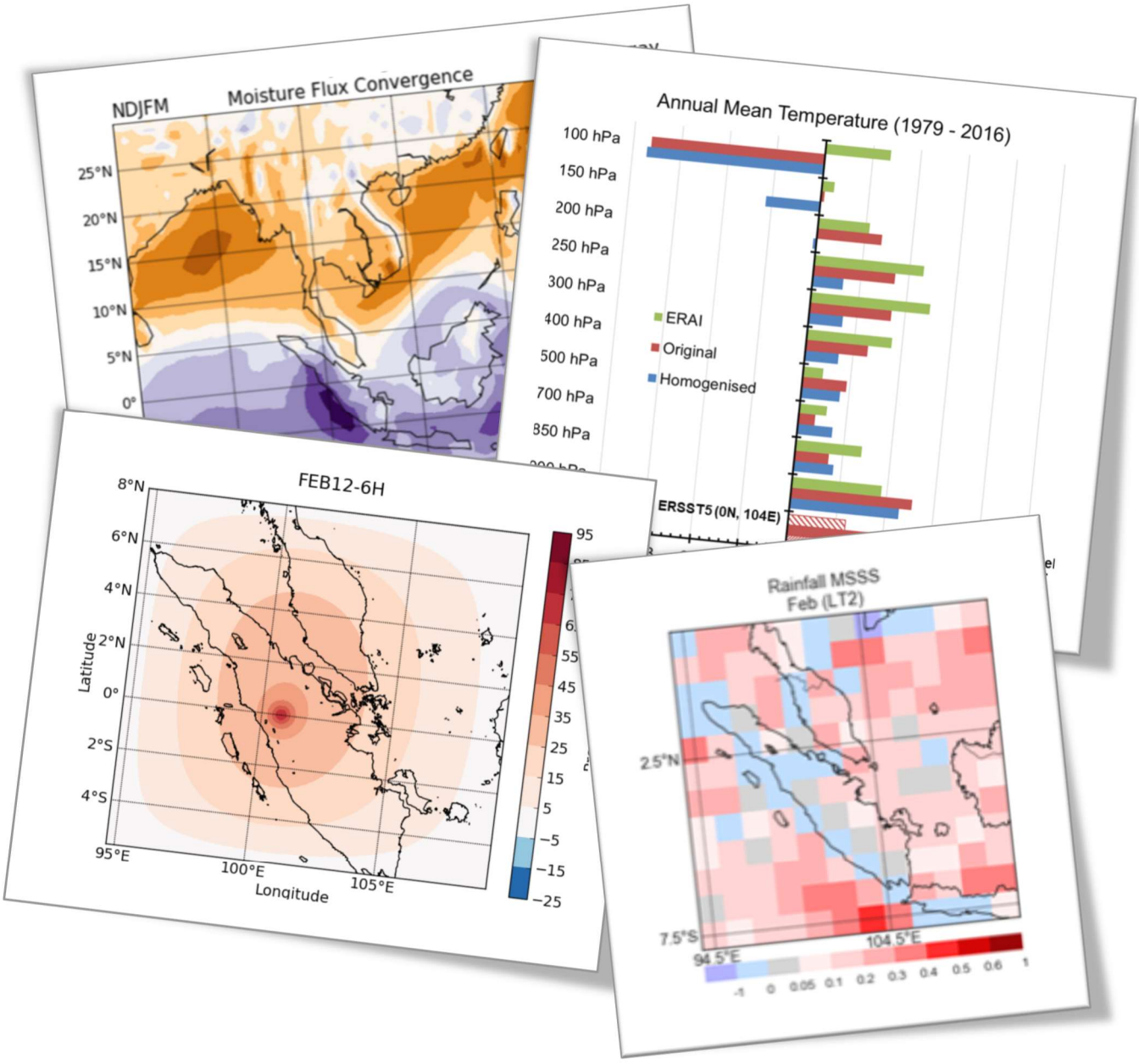

MSS Research Letters

Issue #3, July 2019

Meteorological Service Singapore

DISCLAIMER OF WARRANTIES AND LIABILITY

1. While National Environment Agency Meteorological Service Singapore (NEA MSS) has made every reasonable effort to ensure that the information contained in this publication has been obtained from reliable sources, NEA MSS shall not be responsible for any errors or omissions, or for the results obtained from the use of such information.

2. NEA MSS shall also not be liable for any damage or loss of any kind howsoever caused as a result of any reliance on the contents of this publication.

EDITOR'S NOTE.

One year after our inaugural issue, I am pleased to present the third issue of MSS Research Letters. This third issue covers four different research topics from the Centre for Climate Research Singapore, with two of the letters building on research from previous issues. Moving on beyond the case studies addressed in Issue #2, the Subseasonal and Seasonal Branch addresses the question as to whether forecasts at the one to four-week time scale are more skilful over land or over the ocean. The importance of cold surges to Singapore was also addressed in the previous issue, and in this issue you can read about how cold surges are related to prolonged wet spells. It is satisfying to see researchers building upon results from earlier issues of MSS Research Letters. And the two new topics in this third issue are no less rewarding. The homogenisation of Singapore's upper-air temperature soundings letter provides an in-depth look at one of the longest upper-air sounding records in the Tropics. The final letter tackles data assimilation in the MSS numerical weather prediction model SINGV – while this is a challenging topic for MSS Research Letters, it is hoped that this letter will provide an interesting introduction to readers less familiar with data assimilation research.

To all the authors and reviewers, I would like to thank you all for working together to provide these interesting contributions. Thank you especially to our external reviewers for this issue: Chris Gordon, Gabriel Lau, and Roberto Buizza. Your contributions to ensure the scientific integrity of the MSS Research Letters and your guidance to improve MSS Research Letters is much appreciated.

To all our readers, both inside and outside Meteorological Service Singapore, we hope you enjoy this issue of MSS Research Letters and will consider submitting suitable material for subsequent issues.

Warm regards,
Thea Turkington
Editor, MSS Research Letters

Cover figures: top left – Climatological vertically integrated moisture flux convergence (A moisture flux perspective on cold surges and wet spells affecting Singapore, page 4); top right – Annual mean temperature above Singapore (Singapore monthly upper-air temperature soundings: homogenisation, trends, and relationship to ENSO, page 19); bottom left – Changes in pressure field due to the shift in a single pressure observation (Structures of the background error covariance matrix for SINGV, page 28); bottom left – Mean squared skill score for weekly rainfall in February based on a 2 week lead time forecast (Subseasonal rainfall forecast skill in Southeast Asia: comparing the land and sea regions around Singapore, page 13)

TABLE OF CONTENTS

A MOISTURE FLUX PERSPECTIVE ON COLD SURGES AND WET SPELLS AFFECTING SINGAPORE

Junhua Yang, Jianhua Qian, and Bertrand Timbal

Climate Modelling and Prediction Section, Centre for Climate Research Singapore, Meteorological Service Singapore

INTRODUCTION

From November to January, rapid strengthening of northeasterly winds over the South China Sea during northeast monsoon cold surges can trigger deep convection in parts of the Maritime Continent (Chang et al. 1979; Change et al. 2006), leading at times to extreme rainfall and floods (Tangang et al. 2008; Wu et al. 2007). These surges are driven by cold air outbreaks triggered by strong pulsations and the southward intrusion of the Siberian-Mongolian high pressure system. Several cold surges are normally observed each boreal winter, with typical durations of 2 to 7 days. Longer durations, while possible, are rare.

A cold surge typically brings prolonged cool and rainy weather over Singapore for several days (Yang et al. 2018). Such wet spells may contribute to significant rainfall amounts that are of interest to water management. They are one of the notable weather events annually reported in Singapore (MSS 2017; MSS 2018).

While anecdotal evidence suggests that major wet spells have always occurred when large-scale cold surges were observed, large-scale cold surges as diagnosed by Lim et al. (2017) do not necessarily result in a wet spell in Singapore. In fact, some of these cold surge events may coincide with dry weather in Singapore and its surroundings. Studying the large-scale features for these different outcomes may provide positive insights for the benefit of weather and climate predictions, as well as for model evaluations. In this study, moisture fluxes and their convergence (commonly used in weather forecasting, see Banacos and Shultz 2005) across the Western Maritime Continent (WMC) are explored. This is an attempt to blend a local perspective on Singapore wet spells with the broader regional perspective of cold surges over the South China Sea in order to improve our understanding of the relationship between the two.

DATA AND METHODS

Large-scale fields were obtained from the European Centre for Medium Range Weather Forecasting (ECMWF) Interim Reanalysis dataset (ERA-I). This reanalysis dataset consists of daily mean values of various atmospheric fields obtained by averaging over 6-hourly data spanning from 1979 to 2018 at a spatial resolution of 1x1 degree (Dee et al. 2011). The atmospheric fields used in this analysis include the horizontal wind components (u, v), the mean sea level pressure (mslp), the vertical integral of the water vapour flux (northward, eastward) and the vertical integral of the divergence of the moisture flux. All vertically integrated products were precomputed using 60 instantaneous analysed model levels from the surface to the top of the atmosphere (0.1 hPa), and were directly available as part of the ERA-I dataset.

Rain-gauge data for Singapore consisted of the daily total rainfall duration recorded by all available stations from 1979 to 2018. The daily total rainfall duration for Singapore was taken to be the maximum rainfall duration measured across all available stations. Rainfall duration was recorded using 5-minute time resolution. In this study, the climatological reference period is 1981–2010.

Cold surge days and events were identified using the method in Lim et al. (2017) (refer to Figure 1 in Lim et al. (2017) and relevant text for details). These cold surges bring wet spells with persistent rainfall over Singapore, which have a higher impact than the short-duration (less than 2 hours) thundery showers that are more commonly experienced.

In this study, wet spell events are defined as at least two consecutive days with daily total rainfall duration exceeding 8 hours. Only 6% of the days during the Northeast Monsoon season meet that 8-hours criteria. The annual distribution of wet spells in Singapore indicates their prevalence during the Northeast Monsoon season, with a peak around December and January (Figure 1a). As expected, these mostly coincide with the occurrence of cold surges (Figure 1b). Wet spells last from 2 to 6 days only, while the duration of cold surge events is longer, the longest event being 31 days from 6 January 1987 to 5 February

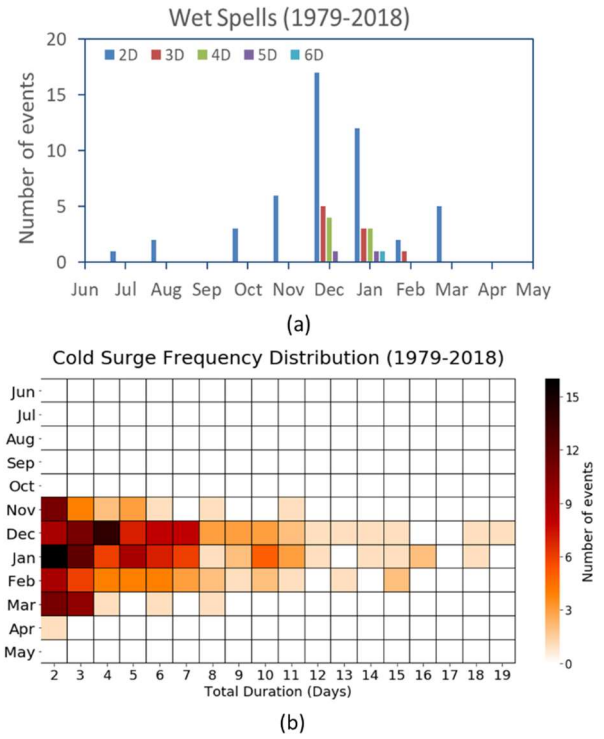

Figure 1 a) Annual frequency distribution of wet spell event durations computed from Singapore observed rainfall from 1979-2018 and b) cold surge event durations, truncated to duration up to 20 days.

1987 (not shown in Figure 1, which only displays events up to 19 days).

The mean (median) duration of cold surge events is 5.4 (4) days, and the standard deviation is 4 days. Seventy-five percent of cold surge events are less than 7 days long. These basic statistics of both wet spells in Singapore and cold surges across the WMC provide some context on the connections between the two events. Clearly, wet spells occur less frequently and are of shorter duration than cold surges.

The moisture fluxes considered are the vertically integrated moisture flux (viMF) and viMF convergence. The viMF vector $\vec{Q}$ at each given longitude and latitude position and time is defined by the following equation:

$$\vec{Q}(\lambda,\phi,t) = -\frac{1}{g}\int_{p_b}^{p_t} q\vec{V}dp = Q_\lambda \hat{\imath} + Q_\phi \hat{\jmath} \qquad (1)$$

where λ, ϕ and t refers to the longitude, latitude and time respectively, g is the gravitational acceleration, q is the specific humidity and $\vec{V}$ is the horizontal wind vector. Q_λ and Q_ϕ are the horizontal components of the flux vector; p_b is the surface pressure and p_t at 0.1 hPa.

viMF gives the magnitude and direction of the net transport of water vapour through the whole column of the atmosphere above a point; it helps identify regions where more water vapour is being transported and also the direction of the flow of water vapour, i.e. its origin. The convergence of viMF ($viMF_{Conv}$) is obtained by computing the divergence of the moisture flux vector $\vec{Q}$, defined by the following equation:

$$\mathrm{viMF_{Conv}} = -\nabla \cdot \vec{Q} \qquad (2)$$

$viMF_{Conv}$ is a useful diagnostic related to precipitation as it captures the net transport of water vapour into (or out) of a point. Water vapour build-up in regions with positive convergence enhances the chance of precipitation, while the opposite is true. This is a very effective diagnostic in relation to rainfall in the wet tropics (Banacos and Shultz 2005; Brubaker et al. 1994).

Results and Discussion

Focussing on the NDJFM season which is the period where most wet spells and cold surges occur, seasonal mean moisture flux (Figure 2) for the reference period (1981–2010) depicts a strong moisture flux over the South China Sea, transporting water vapour towards Peninsular Malaysia, Singapore and southwards towards Sumatra and Java. The positive convergence

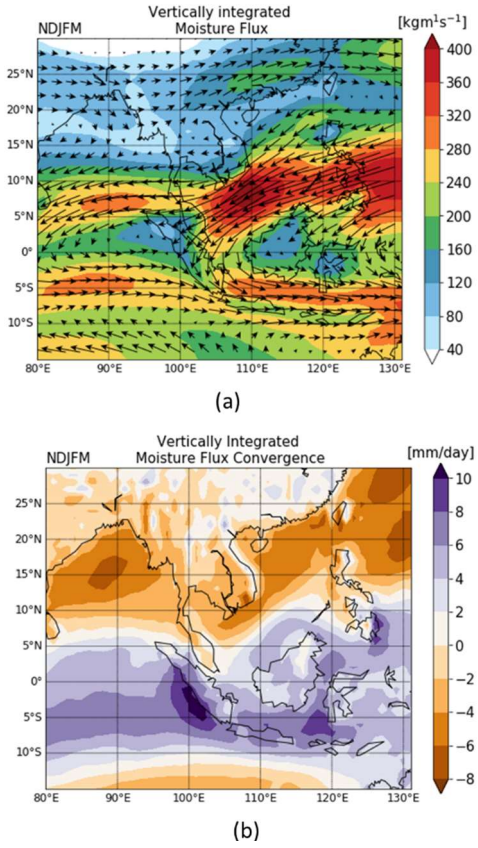

Figure 2 a) Seasonal mean of the Vertically Integrated Moisture Flux b) the corresponding convergence pattern during the Northeast Monsoon season (NDJFM). The seasonal means are computed for the climatological reference period from 1981 to 2010.

from 5°N to 8°S is the mean location during this season of the meteorological equator, which indeed is named the Inter Tropical Convergence Zone (ITCZ). Regional features of interest include an area of weak moisture convergence within the ITCZ at the southern end of the South China Sea, suggesting that the strong flow transports the moisture further south, leading to a strong area of convergence south of Borneo. Other areas of strong convergence appear linked to orography: there is an area of strong northeasterly viMF east of the Mindanao archipelago, and also west of Sumatra where westerly and northeasterly viMF fluxes converge. Besides the mean state, anomalies in these moisture flux patterns in relation to cold surges and wet spells are also the focus of the analysis.

The degree of overlap between the cold surge days and wet spell days is illustrated in a Venn diagram (Figure 3) which identifies the number of days falling into four distinct categories. A majority of Singapore's wet spell days coincide with cold surges (68%: 104 out of 153). These 104 days are only a small fraction of the entire cold surge days (9% out of 1128 days). In fact, the majority of the cold surges (85%: 956 out of 1128) are normal cold surges that are generally wet but not sufficient to trigger a wet spell. It is noteworthy that within the cold surge days, up to 6% (68/1128) are classified as dry surges. These dry surge events are defined as those not leading to wet spells and where Singapore experiences no rainfall for at least half of the total duration during each event.

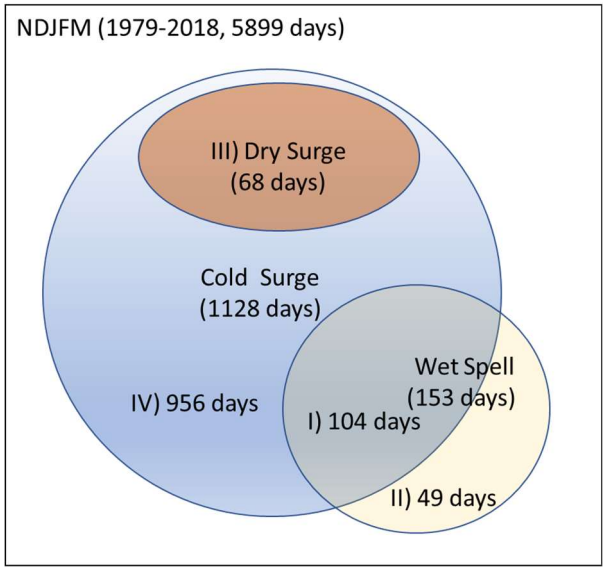

Figure 3 Venn diagram illustrating the overlap of cold surge days and the local wet spell days observed in Singapore during the NDJFM season. Four major situations of interest (I, II, III, and IV) are labelled in the Venn diagram together with the total number of days in each situation.

The differences between these 4 categories in terms of meteorological conditions are explored by computing composites of the viMF patterns corresponding to the four situations in the Venn diagram (Figure 3) for both flux anomalies (top) and the anomalies of convergence (bottom) (Figure 4). When Singapore is affected by a wet spell during a cold surge (i.e. situation I), a strong positive moisture flux anomaly develops over the South China Sea with a prominent "V-shaped" positive moisture flux convergence anomaly from the Bay of Bengal to the Malay Peninsula and the South China Sea, with the strongest positive convergence anomaly between Singapore and western Borneo.

In the case of wet spells when no cold surge is observed (situation II), the moisture flux anomaly across the South China Sea is weaker and less extensive. The area of strong positive convergence anomalies is very localised next to Singapore and weaker across the equatorial South China Sea. A very significant difference in situation II as compared to situation I is the presence of positive instead of negative convergence anomalies around Hainan Island, southeastern China, and Taiwan region. That means that the negative convergence anomalies for situation I that indicated an outflow of moisture due to the cold air outbreak from the Siberian-Mongolian high pressure system are not present in situation II.

In the case of cold surges associated with dry weather (situation III), the cold surge across the South China Sea appears weak with positive moisture flux anomalies limited to the South China Sea and not extending past the Malay Peninsula. There is also less water vapour passing through the Singapore region as compared with other situations. As a result, negative moisture convergence anomalies suppress precipitation around Singapore and the surrounding region.

Finally, the majority of those cold surges that are neither "dry" nor "wet" (situation IV) display a spatial extent of the positive moisture flux anomaly pattern similar to the "wet" surge days, but weaker in magnitude. Similarly, the "V-shaped" convergence anomaly is weaker. Across the entire domain, the magnitude of the convergence anomalies is weaker compared to the "wet" cold surge (situation I).

During cold surges, air-sea interaction over the South China Sea plays an important role in modulating the moisture transport in the region. The cold and dry continental air warms and picks up moisture and becomes convectively unstable as it flows over the warmer South China Sea towards the equator. The strong wind and large temperature contrast between

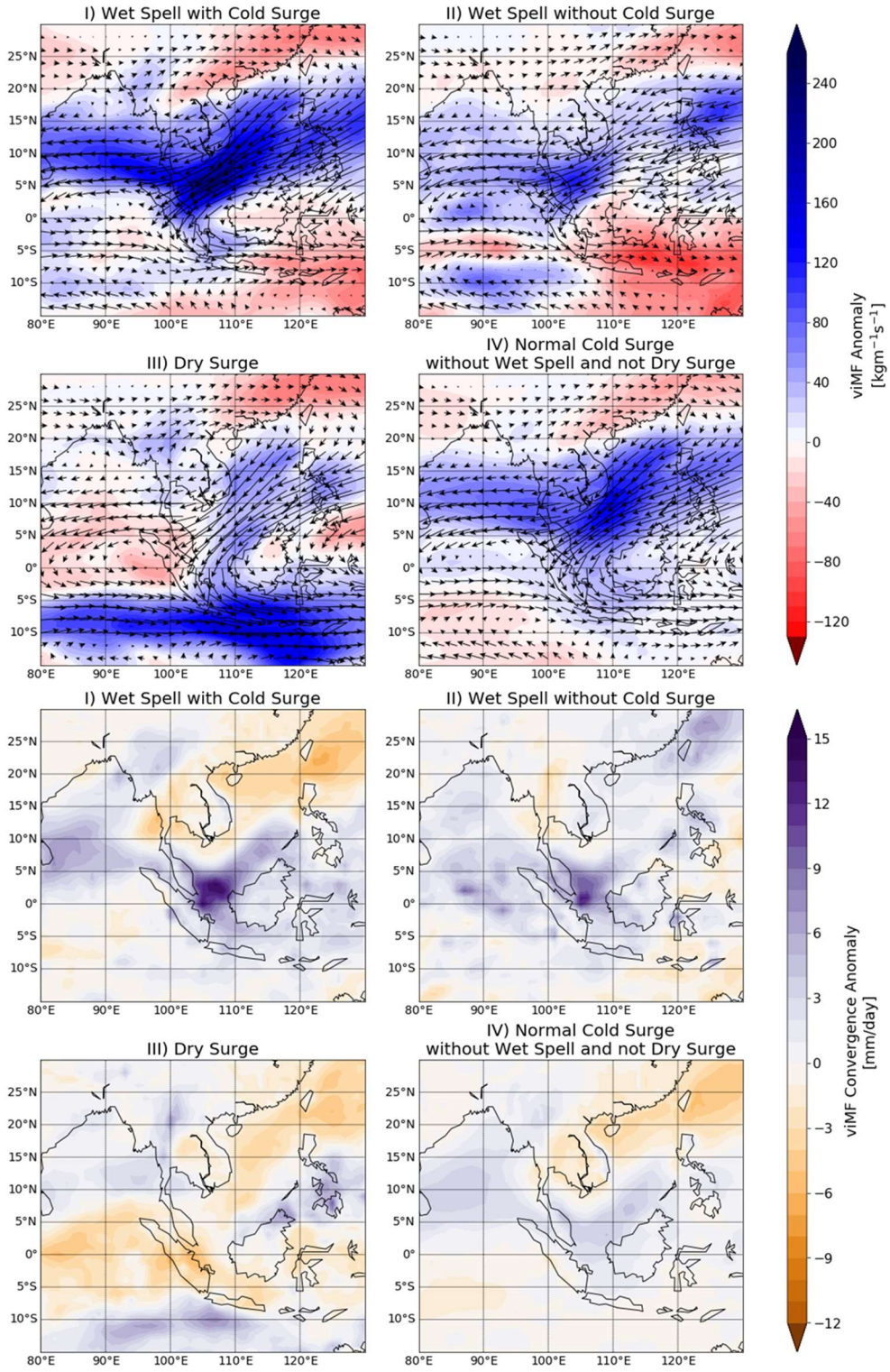

Figure 4 Top panel: the composite mean of the moisture flux anomaly for the four situations of interests. The shading refers to the magnitude and sign of the anomaly. The directions of the arrows give the directions of the anomaly flux vectors. Bottom panel: corresponding moisture flux convergence anomaly.

the air-sea interface enhances the evaporation rate and the upward flow of sensible heat flux from the sea to the air aloft. The air-sea interaction appears to be especially strong during “wet” cold surges, leading to a strong positive moisture flux anomaly in the South China Sea, and is much weaker during a “dry” surge (Figure 4).

From a forecasting perspective, besides the diagnostic in real time of differences in mean meteorological conditions corresponding to these various situations, early signs in the genesis of these differences, if any, are relevant. The lagged composite mean moisture flux anomaly patterns leading to wet spells in Singapore during cold surges were computed

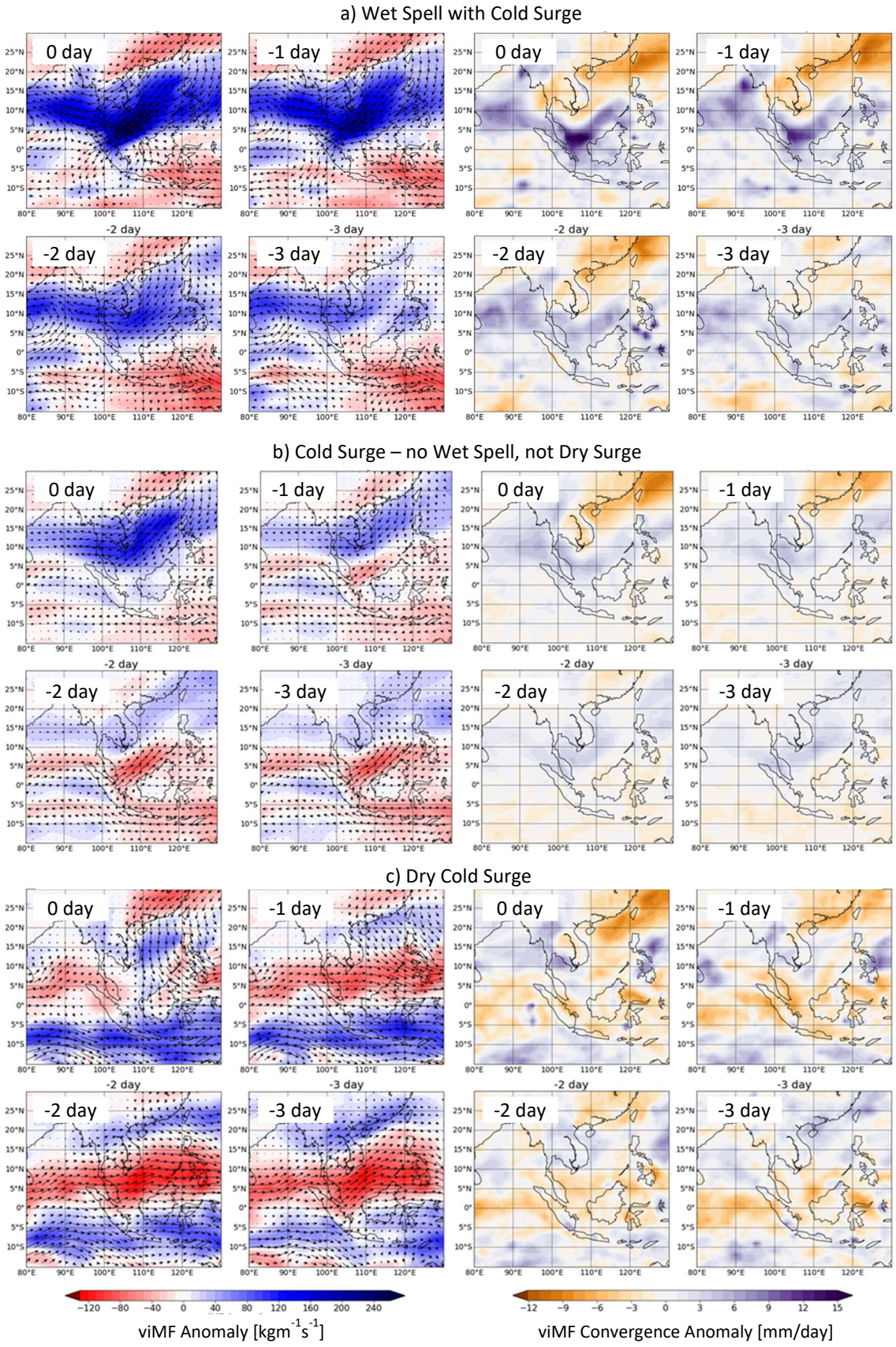

Figure 5 Lagged mean moisture flux (left) and convergence (right) anomalies (from day 0 to day -3) for: a) I: "wet" cold surges based on 32 past events; b) IV: normal cold surges (no wet spells) based on 208 past events; and c) III: "dry" cold surges based on 19 past events.

for all four situations and shown for three situations (Figure 5). The plots are not shown for situation II (wet spells without cold surge) due to the small sample size to construct the composite and the lack of obvious patterns.

In the case of "wet" cold surges (Figure 5a), a clear strengthening of the moisture flux in the South China Sea starting two days before the start of the wet spell is noticeable, and is reinforced on day 0 by a cyclonic circulation between Singapore and western Borneo. Also, two days before the start of a wet spell, a negative moisture flux convergence anomaly appears in areas around Hainan Island, southeastern China and Taiwan, clearly in relation to a sizeable cold air outbreak from further north in East Asia. This appears as a precursor signal (by one day) forcing water vapour to converge further downstream across the South China Sea, with the positive "V-shaped" convergence anomaly slowly emerging from day -2 to day 0. Most of the anomalies described above for day -2 are also present at day -3 (and in fact up to day -5, although this is not shown). However, these are much fainter and therefore less likely to be useful from a forecasting perspective.

The lagged composite plots for the normal rainfall cold surges (situation IV) are computed for 208 events (Figure 5b). Overall, the moisture flux and convergence anomalies resemble situation I, albeit weaker and shifted to the north, and affecting the northern part of Peninsular Malaysia and Thailand instead of Singapore. Noticeably, the moisture divergence along the southeastern coast of China emerges only the day before the start of the cold surge, indicating a weaker cold air outbreak from the north across East Asia. In this situation, Singapore would most likely experience the usual wet weather from a cold surge but lacking the rainfall duration criteria to constitute a wet spell.

Finally, the "dry" cold surges composite (Figure 5c) is only computed from 19 events, and hence may not be robust. However, it remarkably does display a strong and persistent belt of negative moisture flux anomalies north of the equator (0°–15°N) and a belt of positive flux anomalies south of the equator (0°–12°S). These features are clear and persistent, and can readily be seen three days before the start of the dry surge (and in fact up to five days prior, although this is not shown). Between the two belts of flux anomalies with opposite sign, negative flux convergence anomaly is widespread between 5°S and 5°N). These drier than normal conditions over the equatorial belt appear stable over time, and are not impacted by the cold surge related anomalies, hence leading to the "dry" outcome of these cold surges. This suggests that they tend to occur at times when the equatorial belt is less active.

It is in fact noteworthy that dry surges occur mainly during the second half of the Northeast Monsoon season (i.e. in January and peaking in February), and are very rare early in the season (November and December). This is in marked contrast to "wet" surges which occur primarily during the earlier half of the Northeast Monsoon season (in December and January) (Table 1).

Table 1 Proportion of "Wet" and "Dry" surges during the NDJFM season corresponding to situations I and III in Figure 3.

1979-2018	Nov	Dec	Jan	Feb	Mar
"Wet" cold surges (Region I)	5%	47%	39%	6%	3%
"Dry" cold surges (Region III)	3%	0%	31%	47%	19%

CONCLUSION

In this study, the connection between wet spells observed in Singapore and the occurrence of cold surges during the Northeast Monsoon season has been documented. Although cold surges are typically associated with wet conditions over Singapore, there were occasions where the rainfall was below-average or near-average. The conditions and precursors of these events were studied.

Past wet spells and cold surge events, and also cases where they overlapped, were identified. To classify these events into "dry" or "wet" cold surges, key composite means of the vertically integrated moisture flux and its convergence anomaly fields were computed. The lagged values of these composites were also explored in order to assess their predictability and the usefulness of this analysis for weather forecasting.

In the case of "wet" cold surges, a clear strengthening of the moisture flux in the South China Sea was observed two days before the start of the wet spell. The development of a cyclonic circulation between Singapore and western Borneo on the day the wet spell began was also observed. In addition, a characteristic "V-shaped" positive moisture flux convergence anomaly from the Bay of Bengal to the Malay Peninsula and the South China Sea was also seen to emerge gradually two days before the start of the wet spell. In contrast, "dry" cold surges exhibited a strong and persistent belt of negative moisture flux anomalies

north of the equator (0°–15°N) and a belt of positive flux anomalies south of the equator (0°–12°S). These were readily seen up to five days before the start of the dry surge. Between the two belts of flux anomalies with opposite sign, a negative flux convergence anomaly was widespread between 5°S and 5°N. These features, however, may not be related to particular meteorological situations as their predictability may simply be related to the time of the year, since these "dry" surges mostly occur late in the season (January and February).

This analysis provides an improved understanding of cold surges, along with an assessment of their associated impact on Singapore. It has also shed some light on their predictability a few days ahead of the cold surge situations defined in this study, which is of relevance to forecasters in Singapore and its surrounding areas.

Future research will include the development of indices for the various cold surges affecting Singapore (wet, normal or dry). These can then be used with output from regional climate models in order to evaluate how these surge episodes can be affected by climate variations across timescales from inter-annual variability to climate change projections.

REFERENCES

Banacos, P., Schulz, D.M. (2005) The use of moisture flux convergence in forecasting convective initiation: Historical and operational perspectives. *Weather and Forecasting*, 20:351–366.

Chang, C.P., Erickson, J.E., Lau, K.M. (1979) Northeasterly cold surges and near-equatorial disturbances over the winter MONEX area during December 1974. Part I: Synoptic aspects. *Monthly Weather Review*, 107:812–829.

Chang, C.P., Wang, Z., Hendon, H. (2006) The Asian winter monsoon. In: *The Asian Monsoon*, Wang, B. Ed., Springer Praxis Books, 89–127.

Dee, D.P., Uppala, S.M., Simmons, J., Berrisford P., Poli, P., Kobayashi S., Andrae, U., Balmaseda, M.A., Balsamo, G., Bauer, P. et al. (2011) The ERA-Interim Re-Analysis: Configuration and performance of the data assimilation system. *Quarterly Journal of the Royal Meteorological Society*, 137:553–597.

Lim, S. Y., Marzin, C., Xavier, P., Chang, C.P., Timbal, B. (2017) Impacts of Boreal Winter Monsoon Cold Surges and the interaction with MJO on Southeast Asia Rainfall. *Journal of Climate*, 30:4267–4281.

Brubaker, K.L., Entekhabi, D., Eagleson, P.S. (1994) Atmospheric water vapor transport and continental hydrology over the Americas. *Journal of Hydrology*, 155:407–428.

MSS (2017) Annual Climate Assessment Report. Available at: http://www.weather.gov.sg/climate-annual-climate-reports, last accessed 13 May 2019.

MSS (2018) Annual Climate Assessment Report. Available at: http://www.weather.gov.sg/climate-annual-climate-reports , last accessed 13 May 2019.

Tangang, F.T., Juneng, L., Salimun, E., Vinayachandran, P.N., Yap, K.S., Reason, C.J.C., Behera, S.K., Yasunari, T. (2008) On the roles of the northeast cold surge, the Borneo vortex, the Madden–Julian oscillation, and the Indian Ocean dipole during the extreme 2006/2007 flood in southern Peninsular Malaysia. *Geophysical Research Letters*, 35:L14S07.

Wu, P., Hara, M., Fudeyasu, H., Yamanaka, M.D., Matsumoto, J., Syamsudin, F., Sulistyowati, R., Djajadihardja, Y.S. (2007) The impact of trans-equatorial monsoon flow on the formation of repeated torrential rains over Java Island. *SOLA*, 3:93–96.

Yang, J., Teo, P.Y., Timbal, B. (2018) Was the Singapore January 2018 cold spell record-breaking? In: *MSS Research Letters Issue 2*, 26–32.

SUBSEASONAL RAINFALL FORECAST SKILL IN SOUTHEAST ASIA:

COMPARING LAND AND SEA REGIONS AROUND SINGAPORE

Wee Leng Tan, Ryan Kang, and Thea Turkington

Subseasonal and Seasonal Prediction Section, Centre for Climate Research Singapore, Meteorological Service Singapore

INTRODUCTION

Subseasonal-to-Seasonal (S2S) forecasts aim to bridge the gap between short-term weather forecasts and longer-term climate predictions. The subseasonal time range is commonly defined to be from 2 weeks to 2 months, and accurate forecasts within this time range provide considerable potential for various sectors, including water management and disaster risk management. Li and Robertson (2015) have noted the potential of S2S forecasts in the Southeast Asia (SEA) region, with forecasts by the ECMWF S2S model providing comparatively good skill in the SEA region as compared to other regions in the world.

The S2S Southeast Asia Capability Building Training Workshop was initiated in 2017 with the aim of introducing S2S prediction to the region's National Meteorological and Hydrological Services (NMHSs) and building up their capabilities thereof. At the first S2S-SEA workshop held in March 2017, temperature and precipitation re-forecasts from the ECMWF S2S model were used to assess the skill in the region (MSS 2017). Preliminary results from this workshop showed that, while the skill of the model in predicting precipitation dropped gradually between forecasts at lead times of 1-week (LT1) to 4-weeks (LT4), some regions retained skill, particularly over the sea.

This letter investigates this hypothesis, assessing whether the ECMWF S2S model is more skilful over sea than land for Singapore and its surrounding region. The period December to February (DJF) was chosen, as the Northeast Monsoon period usually brings heavy rainfall to many parts of Southeast Asia, including Singapore. Therefore, accurate and reliable predictions in the subseasonal time range for this period would be beneficial for many end users.

DATA AND METHODOLOGY

The ECMWF S2S model (Vitart 2014; Vitart et al. 2017) was used in this study. This model is initialised every Monday and Thursday, producing 51 ensemble member forecasts up to 46 days into the future. Twenty years of re-forecasts are also produced starting on the same day of the year as the forecast, each consisting of 11 ensemble members. Re-forecasts are similar to forecasts, but initialised for past dates using reanalysis data. These re-forecasts are used for assessing the model's skill and calibrating the model against its climatology. Re-forecasts can also be used for analysing case studies using a newer version of the model. As ECMWF forecast data is only available from 2015 onwards, only the re-forecast data were used.

Table 1 Summary of data used for this study. The original resolution of the ECMWF S2S model varies between 0.25° and 0.5° (Vitart et al. 2017), although 1.5° resolution is available from the S2S Database.

	Spatial resolution	Temporal resolution	Temporal coverage
ECMWF (re-forecasts)	1.5°	Daily	1995–2016
TRMM	0.25°	Daily	1998–May 2015

Tropical Rainfall Measuring Mission satellite observations (TRMM; Huffman et al. 2007) were used for the verification of the ECMWF model. TRMM version 3B42 v7 was used, which is based on a variety of sensors and sources, including the TRMM Precipitation Radar (Huffman et al. 2007). A summary of the spatial and temporal resolution and temporal coverage for the TRMM dataset, as well as the S2S ECMWF model, can be found in Table 1. Due to the difference in spatial resolution between the TRMM and ECMWF model, the TRMM data was interpolated from 0.25° to 1.5° resolution using linear interpolation.

Weekly re-forecasts were computed at four lead times. Lead time 1 refers to the re-forecast from

the start of the first week (the first seven days of the re-forecast), LT2 refers to the re-forecast initialised the week prior (days 7 to 14 of the re-forecast), and so on up to LT 4 that refers to the re-forecast initialised three weeks prior to the start of the first week (days 21 to 28 of the re-forecast). Figure 1 outlines the initialisation dates for an example week of 4-10 December 2016.

Verification of the model was done using weekly anomalies rather than weekly total rainfall. Using rainfall anomalies removes any shift in the mean values due to model bias. The weekly anomalies were calculated using:

$$a = r - \bar{r} \qquad (1)$$

where a is the weekly anomaly, r is the weekly rainfall total and $\bar{r}$ is the average weekly total (1998–2014). In the case of the re-forecasts, the 11 ensemble members were first averaged before calculating the weekly anomalies and climatologies.

Two skill scores were used: the correlation of anomalies (CORA) and mean square skill score (MSSS; Wilks 2011). CORA, also called the anomaly correlation coefficient, measures the linear association between the predicted anomalies and the observations. Therefore, CORA measures the relative association between the variables, rather than the overall accuracy of the forecast. CORA is also sensitive to outliers (Wilks 2011). CORA varies between 1 (perfect correlation or association) and -1, and was measured using:

$$CORA = \frac{\sum(a_{re})(a_{ob})}{\sqrt{(\sum {a_{re}}^2)(\sum {a_{ob}}^2)}} \qquad (2)$$

where a_{re} is the re-forecast ensemble mean anomaly and a_{ob} is the observed anomaly. The MSSS is based on the mean square error, where the maximum value is 1 for a perfect forecast, and a negative value implies that the re-forecast is less skilful than the climatology. The MSSS can be split into two components: the square of the correlation coefficient (CORA) and the squares of the conditional and mean biases. The conditional biases are those that are dependent on the forecasts, assessing whether, when the forecasts are wet (dry), the observations are also wet (dry) by a similar amount. When using anomaly values, the mean bias has been removed, and MSSS can be calculated using:

$$MSSS = 1 - \frac{\sum(a_{re}-a_{ob})^2}{\sum {a_{ob}}^2} \qquad (3)$$

The skill scores (Eqns. 2 and 3) were calculated independently for each month due to potential seasonal differences in skill. To derive the monthly score, the skill scores were calculated for each week of the month and then averaged, using only weeks that were entirely contained within a month. Therefore, in the example shown in Figure 1, the re-forecasts covering the week 27 November - 3 December 2016 would not be included in either the November or December average skill scores.

The region for the land/sea skill comparison covers 7.5°S – 10.5°N and 94.5°E– 112.5°E, with Singapore in the centre (Figure 2). This region is affected by heavy rainfall during the Northeast Monsoon (DJF). The land-sea mask (Figure 2) shows the regions defined as land and sea in the grid resolution of the re-forecasts. A total of 32% of the grids are considered land, the

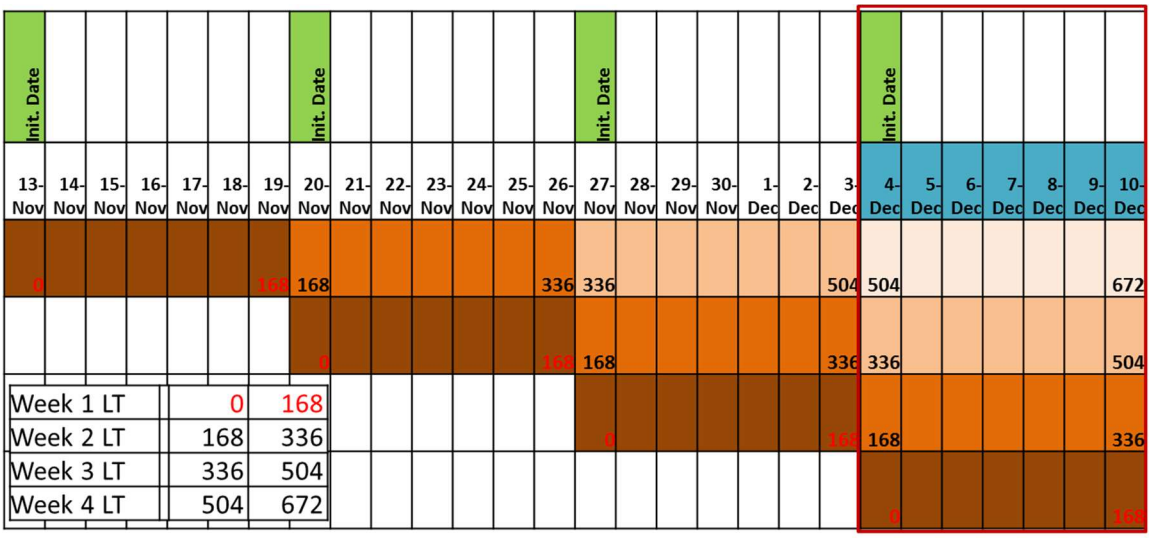

Figure 1 Calendar showing the different initialisation dates for the same period of interest (in red box starting from 4 December 2016). A total of four different initialisation dates are needed for the four lead times for this week. The numbers in the boxes show the hours from the start of initialisation. The four shades of brown refer to the various lead times.

remainder being ocean which, at 68%, makes up most of the area.

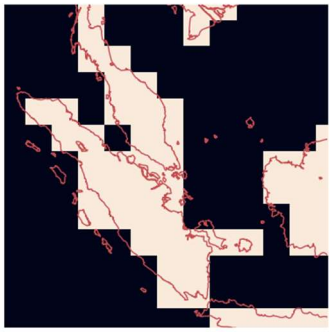

Figure 2 Land-sea surface mask for Singapore and the surrounding region. Black shows the sea region. 32% of the region is demarcated as land surface.

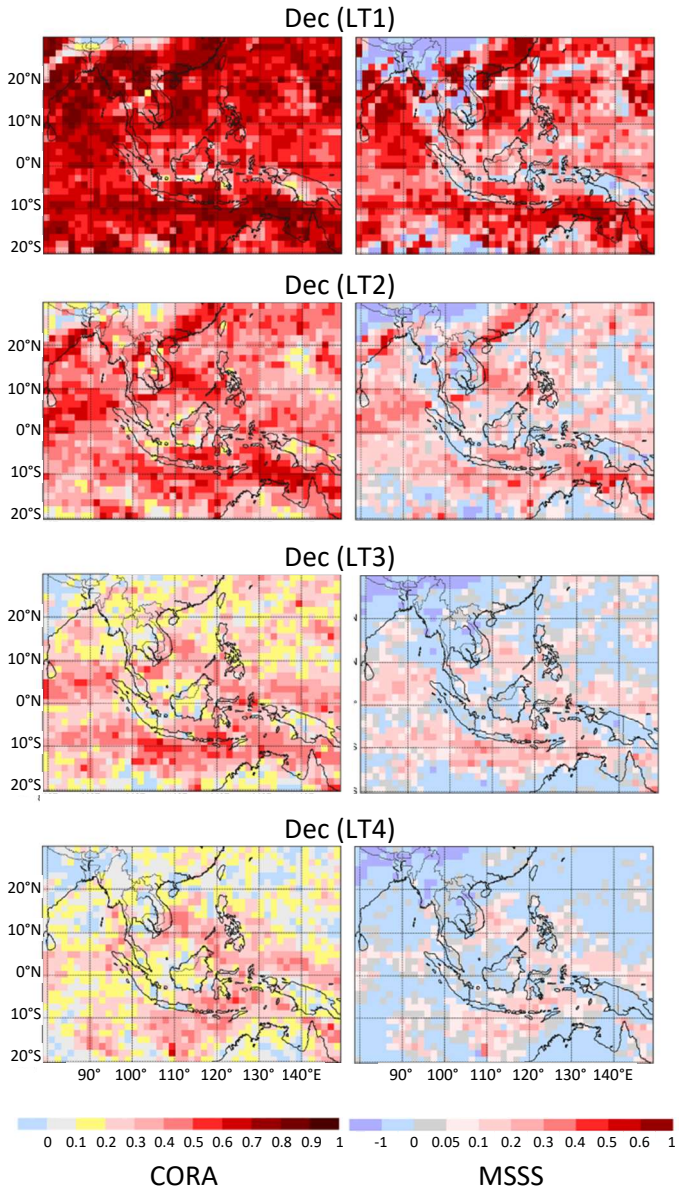

Figure 3 CORA skill score plot for December for LT1 to LT4 (left). MSSS skill score plot for December for LT1 to LT4 (right).

RESULTS

SKILL SCORE MAPS FOR SOUTHEAST ASIA FOR DECEMBER

Figure 3 shows the skill scores, CORA and MSSS, for December, with similar results obtained for January and February (not shown). The colour scheme follows that of Li and Robertson (2015); a CORA value of 0.2 is statistically significant with a p value of 0.05 (based on 101 degrees of freedom: 6 initialisation dates per month for 17 years of hindcasts). For MSSS, values less than -1 (purple) indicate that the re-forecasts are less skilful than climatology. For both MSSS and CORA, red indicates higher skill. In general, all months of DJF show good skill from the ECMWF model at LT1 throughout the region, with some areas showing much higher skill. At LT2, there is statistically significant correlation between the re-forecasts and observations for most of Southeast Asia. However, for regions such as parts of Continental Southeast Asia, the low MSSS values indicate that the re-forecasts are not more skilful than climatology when also taking into account conditional biases. The skill generally continues to diminish with lead time, with LT4 showing low skill in most regions using CORA and MSSS.

SKILL SCORE MAPS FOR SINGAPORE AND THE SURROUNDING REGION FOR INDIVIDUAL MONTHS OF DJF

Focussing on Singapore and the surrounding region, all months of DJF are skilful at LT1, although there is some variation in skill depending on the location and month (Figure 4). This variation is especially clear for December, with lower scores over Sumatra than the rest of the region. The sea region to the west of Sumatra shows comparatively higher scores. There is more skill over the Malay Peninsula for February.

At LT2, the skill has diminished slightly (Figure 5). The spatial distribution of skill tends to maintain a similar pattern to LT1, with lower skill for Sumatra compared to the sea to its west. However, the higher skill for the Malay Peninsula in February decreases more drastically at LT2, and is similar to the skill for this region during December and January. This variation between LT1 and LT2 demonstrates that a higher skill in shorter lead time does not mean the skill will remain for a longer period of time, as the decay in skill is space and time dependent. As for LT3 and LT4, the skill is low and not significant (not shown).

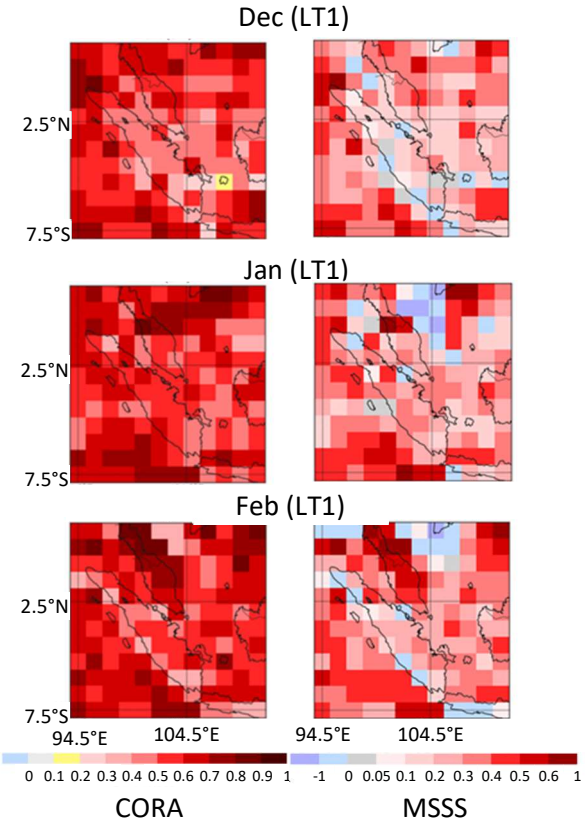

Figure 4 LT1 skill scores for December, January, February for CORA (left) and MSSS (right).

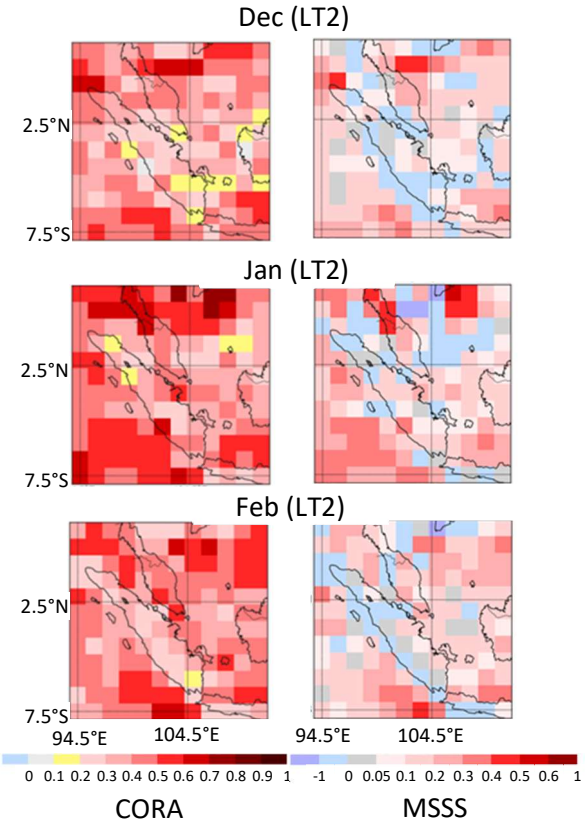

Figure 5 LT2 skill scores for December, January, February for CORA (left) and MSSS (right).

The percentage of grid data points in the area of interest with 'good' skill was calculated by counting the number of grid points with CORA value of 0.6 and above or MSSS value of 0.2 and above, and calculating the percentage relative to the total number of grid points. The value of 0.6 was chosen for CORA as it has been empirically observed to be a reasonable threshold for useful synoptic-scale forecasts (Wilks 2011). As such, the percentage of points above each threshold provides a quantitative measurement of the skill of the model.

Figure 6 shows the percentage of data points with CORA greater or equal to 0.6 and MSSS greater or equal to 0.2. Both CORA and MSSS were consistent in showing a decrease in the number of grid points with good skill with lead time, with LT1 displaying a much higher percentage of grid points with good skill. The decrease in skill appears to be related to the lead time; LT3 and LT4 display almost no points with good skill, except for a small number of such points in LT3 from MSSS. Comparing the three months, December has the lowest percentage of skilful points. At LT1, January and February have similar percentage scores, but at LT2, January has a noticeably higher percentage score than the other two months, especially with regard to MSSS.

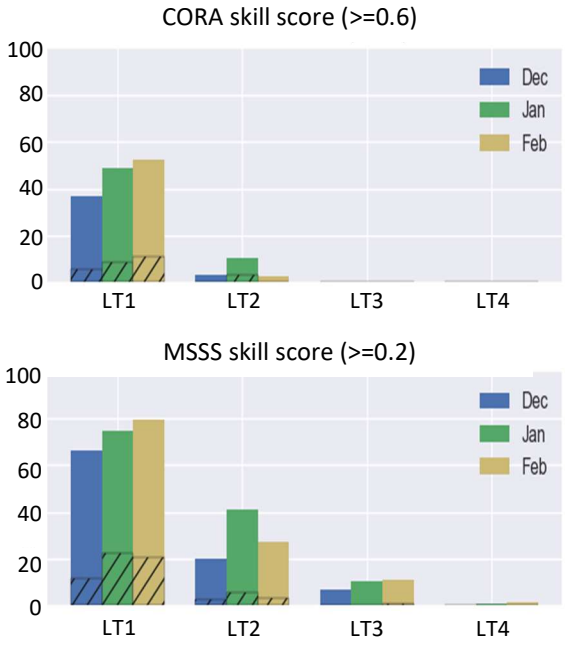

Figure 6 Percentage of points with good skill for December to February from LT1 to LT4, with CORA above and MSSS below. Contribution from the land region is shown in slashes.

Comparing Land and Sea Regions

The slashed lines in Figure 6 show the contribution of the land region to the percentage of

good skill. Table 2 provides the percentage of land grid points contributing to the total number of grid points with good skill. The contribution to the number of points with good skill by the land region is lower than the percentage of land points in the region (32%). The CORA results show an average of 18% of contribution from land for LT1, with February displaying a higher percentage (21%) as compared to December (15%). In the case of MSSS, January has the highest percentage of 30% for LT1, and December again the lowest.

Table 2 Percentage contribution of land regions compared to the total region of good skill.

	CORA (>=0.6)		MSSS (>=0.2)	
	LT1	LT2	LT1	LT2
Dec	15%	0%	18%	14%
Jan	17%	33%	30%	13%
Feb	21%	0%	26%	12%

At LT2, the percentage contribution of the land region drops. Skill for land regions in December is low with 0% for CORA and 14% for MSSS. The result is mixed for January, with CORA increasing to 33% and MSSS decreasing to 13%. For February, the percentage decreased to 0% and 12% for CORA and MSSS, respectively.

In comparison, the deterioration in skill for the sea region is not as drastic as for the land region, with skill generally maintained, especially off Sumatra and in the South China Sea. This result indicates that the skill for the sea region tends to remain for longer lead times than over land.

DISCUSSION

December has the lowest skill, and this is consistent for both LT1 and LT2. From LT3 onwards, all three months have poor skill. The poor skill in December could be due to the onset of the Northeast Monsoon usually occurring during this month in the region around Singapore. It is also the month when this region experiences the strongest cold surges (Lim et al. 2017) which is a phenomenon that may be challenging for prediction at the subseasonal timescale (Toh et al. 2018). In January, there is a weakening of cold surge winds and rainfall anomalies associated with these surges, at which time the Northeast Monsoon is well established. This higher level of skill in January is maintained in LT2, unlike the other two months.

The terrain in Sumatra is highly variable, with higher elevation compared to the surrounding region. This complex terrain is not well represented in the forecast model and it can also impact the observational estimates from TRMM, which are less accurate for mountainous regions. In comparison, the other land regions in the area tend to be relatively flat except for a smaller region of the Malay Peninsula. The latter gives higher skill scores than Sumatra possibly due to its location, as it is more directly affected by strong winds from the South China Sea. Thus, the lower skill score computed for Sumatra could be due to the model and/or the observational data accuracy.

Based on these results, the model displays higher skill over the sea, and this skill also tends to be more persistent as compared to land regions. However, end-users are usually more interested in applications that use rainfall forecasts over land, for example for water resources management and disaster risk management. Therefore, at longer lead times over the coastal areas, it may be useful for forecasters to use the forecasts over the neighbouring sea areas to anticipate the probability of heavy rainfall, rather than to directly use the rainfall forecasts over the land.

There is also potential to increase the value of subseasonal forecasts by further processing the output, such as using Model Output Statistics (MOS). In this study, correction was only done for the mean bias in the re-forecast data, before calculating the skill scores. Low MSSS values could also be caused by conditional biases, which could potentially be corrected (such as forecasted rainfall exhibiting variability that is too high). In particular, regions where CORA values show good correlation but MSSS values are low imply that the MSSS low scores come from conditional biases. However, CORA is sensitive to outliers. Therefore, further study is needed to confirm whether MOS can increase the value of subseasonal forecasts in Singapore and the surrounding region.

In this letter, subseasonal skill was assessed based on the re-forecast data rather than the forecast data, as only four years of forecast data were available. For the ECMWF S2S model, the forecast ensembles are larger than those for re-forecasts (51 members and 11 members, respectively). A larger number of ensemble members suggests that the forecasts may be more skilful than the re-forecasts; although this is expected to affect probabilistic skill scores more than the deterministic skill scores assessed here (Vitart et al. 2014). Re-forecasts are initialised using reanalysis data, which could also affect the difference in accuracy between re-forecast and forecast skill. Therefore, while

re-forecasts are used to assess skill (e.g. Li and Robertson 2015; Vitart et al. 2014), this skill may differ slightly from the forecast skill, with the forecast skill likely to be higher (Vitart et al. 2014).

CONCLUSION

This study verified the ECMWF S2S re-forecasts of precipitation for the region around Singapore up to a lead time of 4 weeks using TRMM observation data. Based on the CORA and MSSS skill scores, it was found that there were clear differences in model skill based on region and lead time. For most areas the more skilful regions tended to remain more skilful with time, although there were some exceptions. It was found that the skill of the region around Singapore was good for LT1 and LT2, with little skill from LT3 onwards. December had the lowest skill of the DJF period.

There was higher skill over the sea region, particularly at LT2. Sumatra had lower skill compared to the other land regions, which could be due to its complex terrain. Therefore, when considering subseasonal forecasts at longer lead times, it is important to observe not only the forecasts over land, often the area of interest, but also the forecasts over sea regions, as re-forecasts over the sea tend to be more skilful.

This study considered only the ensemble mean deterministic forecasts. Future work could include probabilistic forecasts which may be more skilful at longer lead times. Similarly, the study could be extended to other regions of Southeast Asia and times of the year to determine if the results presented here are applicable to all of Southeast Asia.

REFERENCES

Huffman, G.J., Bolvin, D.T., Nelkin, E.J., Wolff, D.B., Adler, R.F., Gu, G., Hong, Y., Bowman, K.P., Stocker, E.F. (2007) The TRMM Multisatellite Precipitation Analysis (TMPA): Quasi-Global, Multiyear, Combined-Sensor Precipitation Estimates at Fine Scales. *Journal of Hydrometeorology*, 8:38–55.

Li, S., Robertson, A.W. (2015) Evaluation of Submonthly Precipitation Forecast Skill from Global Ensemble Prediction Systems. *Monthly Weather Review*, 143:2871–2889.

Lim, S. Y., Marzin, C., Xavier, P., Chang, C., Timbal, B. (2017) Impacts of Boreal Winter Monsoon Cold Surges and the Interaction with MJO on Southeast Asia Rainfall. *Journal of Climate*, 30:4267–4281.

MSS (2017) Concept note for the first S2S-SEA workshop. Available at: https://www.wmo.int/pages/prog/arep/wwrp/new/documents/SEA_S2S_Concept_Note_ver3_Singapore_2017.pdf, last accessed 1 April, 2019.

Toh, S.X.M, Turkington, T., Tan, M.L., Rahmat, R. (2018) Subseasonal forecasting of major wet spells in the southern Malay Peninsula. In: *MSS Research Letters Issue 2*, 18–25.

Vitart, F. (2014) Evolution of ECMWF sub-seasonal forecast skill scores. *Quarterly Journal of the Royal Meteorological Society*, 140:1889–1899.

Vitart, F., Ardilouze, C., Bonet, A., Brookshaw, A., Chen, M., Codorean, C., Déqué, M., Ferranti, L., Fucile, E., Fuentes, M., et al. (2017) The Subseasonal to Seasonal (S2S) Prediction Project Database. *Bulletin of the American Meteorological Society*, 98:163–173.

Wilks, D.S. (2011) Statistical methods in the atmospheric sciences, 3rd edition. Academic Press, Elsevier, San Diego, California, USA.

SINGAPORE MONTHLY UPPER-AIR TEMPERATURE SOUNDINGS: HOMOGENISATION, TRENDS AND RELATIONSHIP TO ENSO

Muhammad Eeqmal Hassim[1], Branislava Jovanovic[2], and Bertrand Timbal[1]

[1]Climate Modelling and Prediction Section, Centre for Climate Research Singapore, [2]Climate Monitoring and Prediction section, Environment and Research Division, Australian Bureau of Meteorology

INTRODUCTION

Daily balloon-borne upper-air observations at 03 UTC commenced in Singapore during the British colonial era on 1 August 1954. After a 9-month interruption, once-daily radiosonde measurements resumed on 1 August 1956 and have since continued uninterrupted with the frequency of ascents changing to twice-daily from 1984. Spanning more than 60 years, the collection of upper-air data from Singapore, located near the Equator, is thus one of the longest and most complete records of continuous upper-air observations anywhere in the tropics. It has been instrumental in understanding large-scale meteorological phenomena, in particular aiding in the discovery of the Madden-Julian Oscillation (MJO), and in the study of the Quasi-Biennial Oscillation (QBO) and equatorial wave activity in the stratosphere (e.g. Madden and Julian 1972; Maruyama 1991; Baldwin et al. 2001).

However, because of changes in equipment (e.g. radiosonde sensor, balloon type, ground receiver) and in launch procedures (e.g. frequency, timing and location), the Singapore upper-air data series, similar to many other upper-air records, is plagued by in-homogeneity. Figure 1 provides a timeline summary of these operational changes at Singapore's upper-air

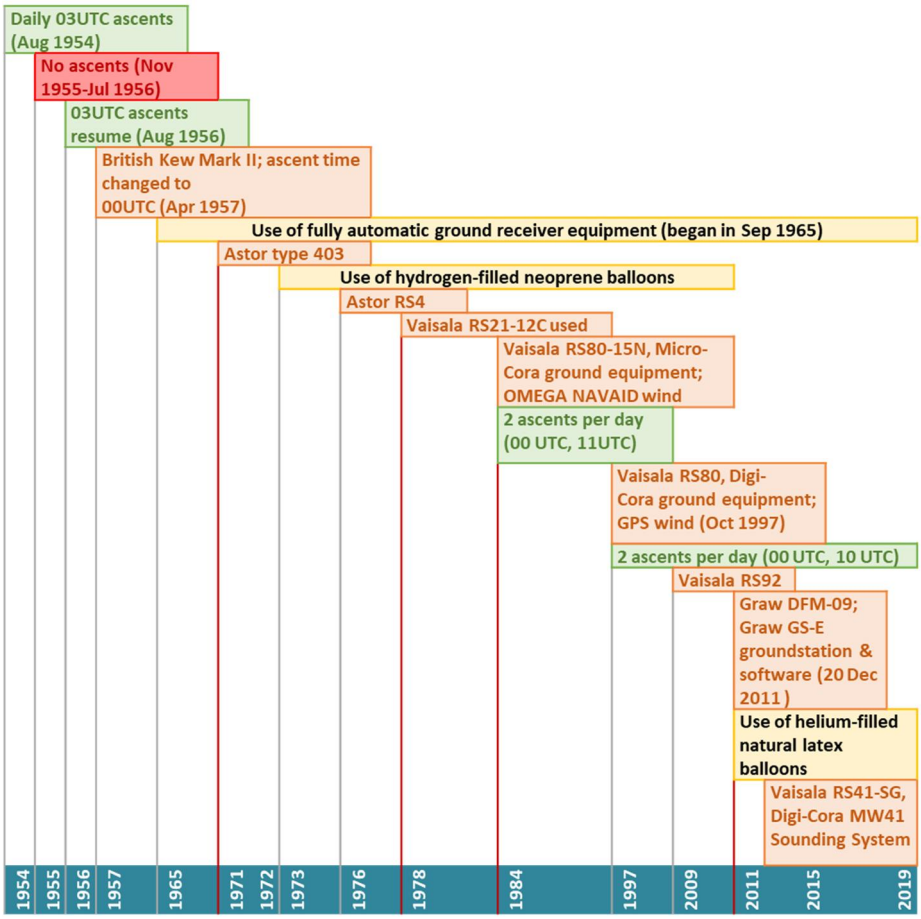

Figure 1 Timeline of changes in Singapore's upper-air operations. Sensor equipment changes are colour-coded in orange. Red lines mark the break points (1971, 1978, 1984 and 2011) detected by the RHTestV3 statistical software package and verified with metadata information. These are the four major break points to which data adjustments were applied (see Table 2).

observation facility. Due to these systematic changes, the raw data cannot provide a reliable estimate of long-term trends in meteorological parameters (e.g. temperature). Thus, many long-term climate studies have relied on vertical soundings from re-analysis products as a proxy for the true observations (e.g. Hassim and Timbal 2019).

In this work, a homogenisation of Singapore's monthly mean temperature data on standard pressure levels was performed, following the method of Jovanovic et al. (2017). The new homogenised time series is then used to 1) characterise the vertical profile of temperature above Singapore; 2) evaluate its long-term trend during a period of global warming; and 3) explore the temperature variability over Singapore in relation to the El Niño Southern Oscillation (ENSO). In the following sections, the data and homogenisation methods used are described, followed by a presentation and discussion of the results before a final summary.

Data and Methods

Radiosonde and surface temperature data

The Upper Air Observatory (UAO) was established in Paya Lebar (1°20'N, 103°53'E) in 1956. Over the years, there have been several changes to the type of sensor and ground receiver used. These are documented in the timeline in Fig. 1 (orange boxes). Depending on the type of radiosonde sensor used, the accuracy of the temperature measurements ranges from 0.15°C (for Vaisala RS21-12C) to 0.2°C (for Vaisala RS80, RS92, RS41-SG and Graw DFM-09) to 0.5°C (Astor RS4). In addition, measurements were taken only once daily at 0000 UTC prior to 1984, after which twice daily observations were made at 0000 UTC and at either 1000 or 1100 UTC.

Since the observations began, the radiosondes have managed to sample the entire troposphere on most days and reached heights of at least 16 km (or around the 100 hPa pressure level), which is near the tropopause. However, with the use of better materials over time, balloon ascents were able to consistently reach altitudes above 30 km in the mid-stratosphere, particularly after 1998 (Figure 2).

For this study, the monthly mean temperature data averaged from daily balloon-borne radiosonde measurements over the 1958-2016 period are used. These data are obtained from the IGRA2 database (https://www1.ncdc.noaa.gov/pub/data/igra), which are provided at 11 standard pressure levels (1000, 925, 850, 700, 500, 400, 300, 250, 200, 150 and 100 hPa). Initial inspections revealed that two years of data (1966, 1967) were missing at most levels, while metadata indicated that there was a change to a fully automated ground receiver in 1965. Due to this equipment change, only data from 1970 onwards were analysed and subsequently adjusted to avoid potential discontinuities.

Surface temperature changes from Paya Lebar and Changi Met Stations were used for reference purposes. Local (0°N, 104°E) and remote (Niño3.4 region 5°S-5°N, 120°W-170°W) sea surface temperature (SST) data were also extracted from the 2° × 2° Extended Reconstructed SST version 5 (ERSSTv5) dataset provided by the National Oceanographic and Atmospheric Administration (NOAA; http://www1.ncdc.noaa.gov/pub/data/cmb/ersst/v5/netcdf/) to examine the relationship of Singapore's tropospheric temperatures to local and remote SST variability. None of these surface time series was subjected to homogenisation.

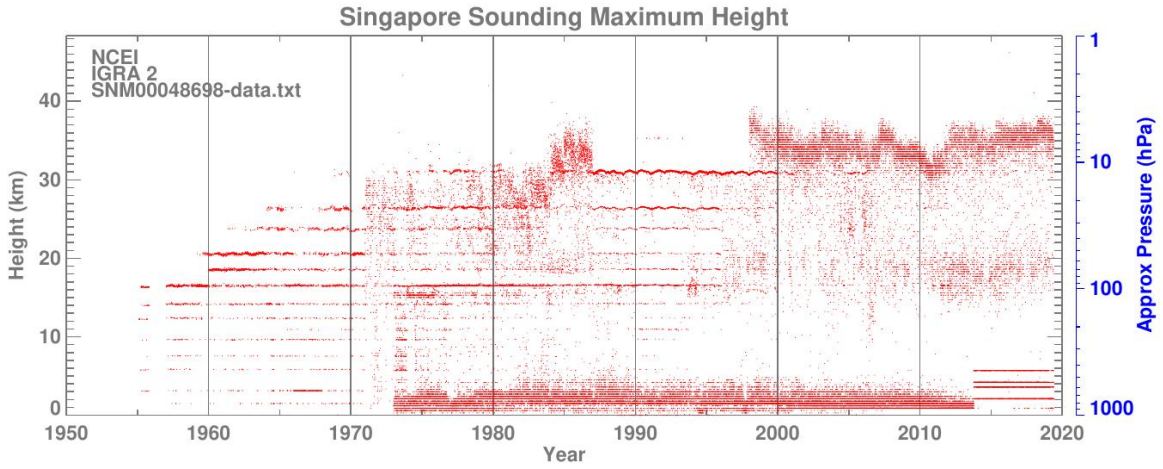

Figure 2 Maximum heights (in km) reached by balloon ascents. The corresponding approximate pressure levels (in hPa) are denoted by the secondary blue axis.

SATELLITE DATA

Gridded (2.5° × 2.5°) satellite temperature datasets from the Remote Sensing Systems (RSS; Mears and Wentz, 2009b,a) and University of Alabama-Huntsville (UAH; Christy et al. 2011) research groups were used as reference series for temperature data between 1979-2016. These homogenised satellite records are derived from brightness temperature measurements made by the Microwave Sounding Unit (MSU)/Advanced MSU (AMSU) sensors for the lower troposphere (TLT), middle troposphere (TMT) and lower stratosphere (TLS). These records are considered as an independent source of upper-atmosphere temperature observations, thus making them suitable to base the bias adjustments on. For our study, satellite temperature data were extracted from the grid point (1.25°N, 103.75°E) closest to the location of the UAO and used as reference. The RSS v3.3 and the UAH v5.6 datasets were used, respectively.

Based on MSU/AMSU Weighting Functions, TLT satellite records were used to test the radiosonde temperature data at 850, 700 and 500 hPa levels. Likewise, TMT records were used for the 400, 300, 250 and 200 hPa levels, while TLS records were used for the 150 and 100 hPa levels.

DETECTION OF INHOMOGENEITIES

Statistical tests for time series homogeneity were conducted with the RHTestV3 software package (Wang and Feng 2007). These tests were designed to detect single or multiple break points in a climate time series. The penalised maximal F test (Wang 2008b) was used in the case without the reference series (i.e., for the whole 1958-2016 period). The t statistic test was applied for the case with the reference satellite series (1979-2016 period) by locating points in the difference data series (radiosonde minus reference) where there is a significant shift in the mean (Wang et al. 2007; Wang 2008a). A 99% confidence level was used when testing without the reference series, while a 95% confidence level was applied with RSS and UAH satellite data as reference series. The detected break points from testing with the reference series are shown in Table 1 for each pressure level.

When backed by metadata information, the statistical tests identified four major break points due to changes in radiosonde sensor type, namely in 1971 (change from Kew Mark II to Astor), 1978 (change to Vaisala RS21), 1984 (change to Vaisala RS80) and in 2011 (change to Graw DFM-09). Some tests suggested a possible discontinuity at 1997 (shift to lower temperatures) but test results were too inconsistent for any adjustments to be supplied to that year. However, the potential discontinuity may have contributed to a lower magnitude of increasing trends at some levels (Figure 3).

DATA ADJUSTMENTS

Temperature data for 1979-2016 were adjusted if the same break points were identified using both the RSS and UAH datasets as reference, and these were supported by the supplied metadata. For temperature data prior to 1979, adjustments were only applied to the break points identified by the statistical

Table 1 Results of testing with RHTestV3 (95% confidence level) with RSS and UAH satellite data as reference series (1979-2016). For the 1000 hPa level, the Singapore/Changi Airport surface temperature series (SNM_Sfc; from IGRA2) and the surface temperature series from Malacca (Malacca_Sfc; taken from https://data.giss.nasa.gov/gistemp/station_data/) were also used for initial comparisons.

Statistical Break Points identified with various reference series				
Level (hPa)	**With RSS TLT**	**With UAH TLT**	**With SNM_Sfc**	**With Malacca_Sfc**
1000	1982, 1998, 2011	1982, 1983, 1998, 2011	1984, 2001, 2012, 2015	1983, 2010
925	1998, 2011, 2013	2011	—	—
850	1984, 1990, 2010	1982, 1983, 1994, 2010	—	—
700	1982, 1983, 1991, 2011, 2016	1979, 1983, 2011	—	—
500	1980, 1983, 1991, 2005, 2012	1980, 1983, 1994, 2012	—	—
400	1979, 1983, 1988, 2011	1979, 1983, 1994, 2012, 2016	—	—
300	1984, 1988, 1996, 1997, 1998, 2000, 2011, 2012	1984, 1995, 1997, 1998, 2011, 2012	—	—
250	1980, 1982, 1984, 1988, 1995, 1997, 1998, 2011	1980, 1982, 1984, 1992, 2011	—	—
200	1980, 1992, 2011	1980, 1983, 1984, 1988, 1992, 2011	—	—
150	1981, 1988, 1993, 1997, 2000, 2005, 2009, 2011	1997, 1999, 2000, 2012	—	—
100	1981, 1982, 2016	1981, 1982	—	—

Table 2 Adjustment factors calculated solely from the temperature series (temp) and from the RSS reference series (RSS) for all four break points supported by the metadata (1971, 1978, 1984 and 2011). Bold values indicate break points that were also identified by the statistical tests.

Adjustments to Break Points supported by meta data				
Level (hPa)	**1971**	**1978**	**1984**	**2011**
100	-0.11 T	**+0.79 T**	**+0.25 T**	**+0.79 T**
			+0.36 RSS	**+0.61 RSS**
850	**+0.01 T**	**+1.10 T**	**-0.37 T**	**+0.45 T**
			-0.29 RSS	**+0.28 RSS**
700	-0.06 T	**+1.25 T**	**-0.50 T**	**+0.49 T**
			-0.42 RSS	**+0.30 RSS**
500	**-0.21 T**	**+1.34 T**	**-0.34 T**	**+0.51 T**
			-0.26 RSS	**+0.33 RSS**
400	**-0.30 T**	**+1.45 T**	**-0.27 T**	**+0.64 T**
			-0.14 RSS	**+0.48 RSS**
300	-0.09 T	**+1.00 T**	+0.11 T	**+0.74 T**
			+0.24 RSS	**+0.56 RSS**
250	-	**+1.13 T**	+0.20 T	**+0.72 T**
			+0.34 RSS	**+0.58 RSS**
200	-0.57 T	**+1.23 T**	+0.10 T	**+0.77 T**
			+0.48 RSS	**+0.77 RSS**
150	-0.43 T	+1.20 T	-0.29 T	**+0.75 T**
			+0.09 RSS	**+0.73 RSS**
100	-0.44 T	+1.53 T	-01.16 T	-0.02 T

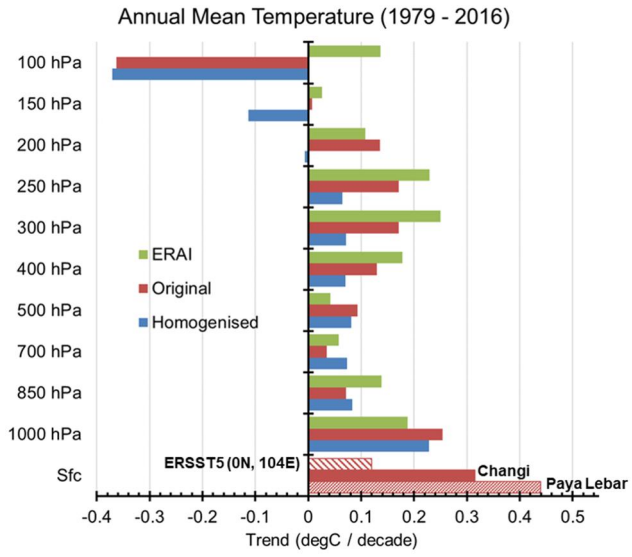

Figure 3 Vertical structure of annual mean temperature trends (in °C / decade) at the surface through to 100 hPa (~16 km altitude), computed from homogenised (blue), original (red) and ERA-Interim (ERAI; green) data, respectively. Surface (Sfc) trends are derived from Changi (filled) and Paya Lebar (hatched) Met Station data, along with local SST data (0N, 104E) from the 2° × 2° ERSSTv5 dataset (diagonals).

tests and supported by the metadata. The adjustments applied are summarised in Table 2.

The adjustments for 1979-2016 were calculated using a difference series, produced by first computing the difference between the tested radiosonde temperature series and the RSS reference series used (i.e. sonde minus satellite). An adjustment factor was then calculated for each month from the difference series, by subtracting the average after the break point from the average before the break point. For the pre-1979 period, adjustments were computed directly from the temperature series, by subtracting the average after the break point from the average before the break point. Note that all results discussed onward are for the 1979-2016 period.

The adjustments were applied to each month. On the annual level, this resulted in a uniform shift which brought each segment of the time series into agreement with the most recent homogeneous section with the assumption that sensors have generally improved over time. This also allowed an easier update of the temperature series.

Trend Estimates

Trends in both the adjusted and original time series are computed at each pressure level by a linear squares fit and tested for statistical significance at the 95% level using regression analysis statistics in Excel. The trends are also compared to those similarly obtained from ERA-Interim re-analysis temperature data extracted from a 0.125° × 0.125° grid point over Singapore (1.375°N, 103.875°E), described in Hassim and Timbal (2019). Temperature trends over the land and sea surface are also calculated using least squares regression.

Results and Discussion

Local Tropospheric Warming Structure

The vertical distribution of observed temperature trends over Singapore (Figure 3) depicts warming in the troposphere above the surface and cooling in the lower stratosphere above the tropopause. This general pattern is consistent with what we expect to occur due to global warming. Noticeably, the actual structure of the local tropospheric warming differs between the adjusted and the original temperature time series. The homogenised data indicate that the atmospheric column over Singapore has undergone fairly uniform heating throughout the free troposphere between 850-250 hPa, with temperatures rising consistently with height at a rate of around 0.06°-0.08°C

per decade. The 'flat' tropospheric warming profile is in stark contrast to the pronounced 'top-heavy' structure obtained from the original temperature data, in which the positive trends increase with height. The latter appear to indicate that the upper troposphere (300-250 hPa) has warmed considerably more than the low-to-middle troposphere (850-500 hPa) with a minimum seen at 700 hPa.

Notably, the data homogenisation has reduced the positive temperature trends between 300-250 hPa by more than 50% of their original values. This reduction suggests that the original radiosonde record had a considerable positive temperature shift (warm bias) in the upper troposphere compared to satellite measurements, which can be attributed to the inhomogeneities caused by systematic changes in the upper-air record. Note that none of the homogenised upper-air data trends, except at 1000 hPa, are statistically significant at the 95% level. This new 'flatter' profile of tropospheric warming is more indicative of a zero or even positive lapse-rate feedback instead of a negative lapse-rate feedback as suggested by the original trends.

The shape of the vertical profile of tropospheric warming derived from ERA-Interim data mirrors that of the original radiosonde data, albeit with stronger heating in the mid-to-upper troposphere (400-250 hPa). However, no cooling trend is seen in the lower stratosphere in ERA-Interim. Notably, ERA-Interim utilises a bias-adjusted global radiosonde temperature dataset known as Radiosonde Observation Correction Using Reanalyses (RAOBCORE_T_1.3; Haimberger et al. 2008) that was derived using difference statistics between the radiosonde temperature time series (obs) and the background (*bg*) forecasts from ERA-40 (prior to 2001) and from ECMWF operational analyses after 2001 (Dee et al. 2011). Interestingly, the *bg* forecasts were used as the reference series for both the change-point detections and the temporal bias adjustments as well. RAOBCORE has been criticised for possible inhomogeneities in the *bg* forecasts, the assumptions made in the assimilating model and for not being independent of satellite observations (Haimberger et al. 2012). Thus, the large differences in upper-level trends between our homogenised data and from ERA-Interim are remarkable but suggest that the tropical tropopause level in the model reanalysis is perhaps much higher than what is observed, possibly because the model convection is too deep and strong. Indeed, it would be worthwhile to compare the vertical structure of trends from our adjusted data with those obtained from another homogenised monthly radiosonde temperature dataset produced using different methods (e.g. Sherwood and Nishant 2015).

Of interest, the 1000 hPa level has been warming at a much faster rate than the levels above (e.g. 850 hPa). This is most likely due to its height (around 100m above the surface) within the boundary layer (typically 1-1.5 km high), thus making it affected by Singapore's on-going urbanisation. Although the 1000 hPa warming trend has been stronger than that exhibited by local SSTs, the strongest warming has occurred at the surface. Between the two long-term surface stations, Paya Lebar has been warming more rapidly than Changi between 1979-2016 (0.44° vs 0.32°C per decade). The more pronounced warming trend at Paya Lebar is a signature of a stronger urbanisation component; over the years, Paya Lebar has developed into an established industrial estate while the Changi site has remained situated on grassland next to Changi Airport since 1984.

In contrast to lower level trends (1000 hPa to surface), the warming at 850 hPa is almost on par with local SSTs. It is commonly accepted that the 850 hPa level is located above the boundary layer and hence, unlikely to be affected by the urbanisation impacting the lower levels. From this perspective, the difference in warming rates between the 1000 hPa and 850 hPa levels can be considered as a simple measure of the time-integrated "island-wide" urban heat island (UHI) effect across Singapore (ignoring lapse rate feedback changes with altitude).

ANNUAL CYCLE OF LOWER TROPOSPHERIC TRENDS

The possibility to infer the characteristic of the island-wide UHI trend is investigated further by looking at the month by month differences in lower tropospheric warming rates (Fig. 4, top). The differences in trends between the two levels are noisy but do show a sustained period from May to August when the differences are smaller; this is most pronounced in August. When compared with the annual cycle of mean wind at 1000 hPa, it shows that this period corresponds to prevailing southerly to southeasterly winds peaking in intensity in August (Figure 4, bottom). It suggests that the maritime nature of the advected air from the south-southeast at this time of the year has contributed to limit the growing UHI effect on the 1000 hPa trend.

The other part of the year when the 1000 hPa wind is strong occurs from December to February. However, it does not correspond to the month when the difference in trends between 850 and 1000 hPa is small. It suggests that at this time of the year, the strong north to northeasterly wind does not have the same effect in

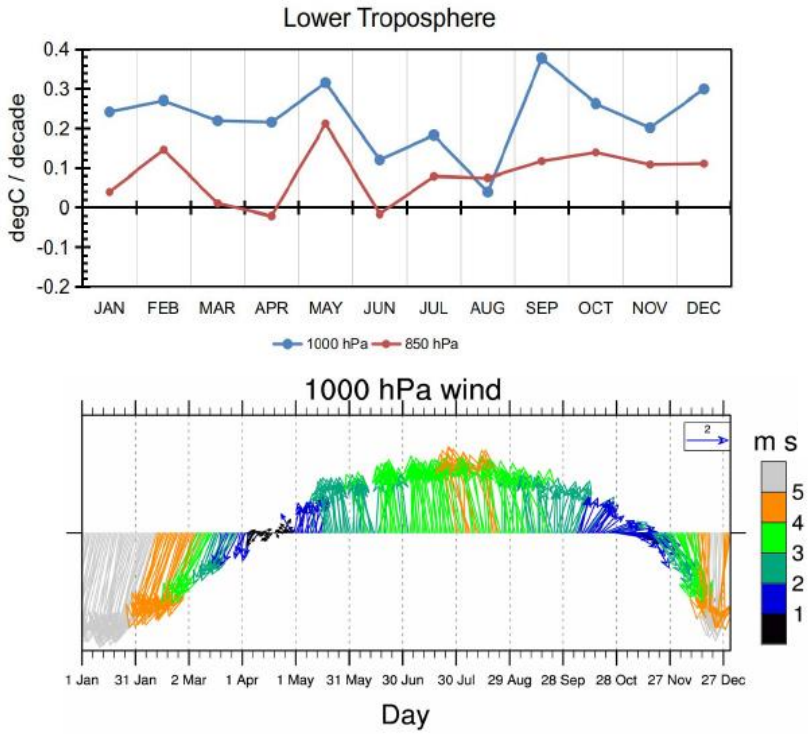

Figure 4 Annual cycle of surface and lower tropospheric (1000 and 850 hPa) trends (top). The annual cycle of the daily climatological wind at 1000 hPa is also shown (bottom).

reducing the growing UHI effect since the wind is blowing from the equally rapidly urbanising part of southern Malay Peninsula (e.g., the city of Johor Bahru).

ENSO INFLUENCE ON SINGAPORE VERTICAL TEMPERATURE PROFILE

As the dominant climate mode of inter-annual variability, ENSO is known to exert a strong effect on surface and tropospheric temperatures globally through remote forcing (Yulaeva and Wallace 1994; Trenberth et al. 2002; Sobel et al. 2002; Chiang and Sobel 2002). A warm ENSO phase (El Niño) contributes to an increase in temperatures both regionally and globally while its counterpart (La Niña) has the opposite effect. Besides remote teleconnections, local SSTs also influence the tropospheric column via direct diabatic processes associated with convection. The newly homogenised vertical profile of temperature offers the possibility to evaluate how the ENSO- vs local SST-related temperature variability operates over Singapore. For this, partial correlations are computed between the adjusted temperature data and the Niño3.4 SSTs by removing the effect of local SSTs. Likewise, the degree of association between the homogenised temperature at various levels and local SSTs is uncovered by removing the influence of the Niño3.4 SSTs. Prior to the correlation analysis, the data are detrended and the mean annual cycle subtracted.

In an annual sense, local SSTs explain more of Singapore's tropospheric temperature (TT) variability than Niño3.4 SSTs, particularly in the middle (850 to 400 hPa) and more prominently in the upper troposphere (300 to 200 hPa) where the relationship with Niño3.4 is much weaker (Figure 5). The shape of the correlation profile between TT and local SST (blue bars) illustrates the role of diabatic heating from tropical deep convection, which is strongly related to local SSTs. The annual correlations are computed using the normal

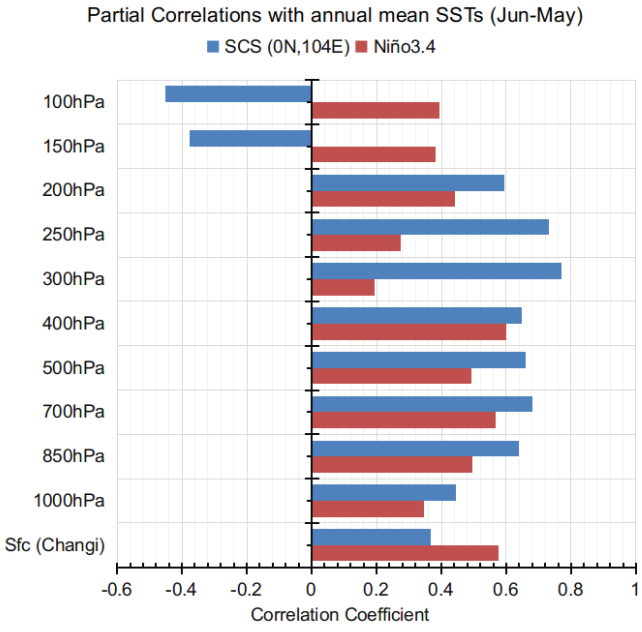

Figure 5 Partial correlations between the annual mean temperature and annual mean local (SCS) and Niño3.4 region SSTs obtained from the Extended Reconstructed SST version 5 (ERSST5) dataset.

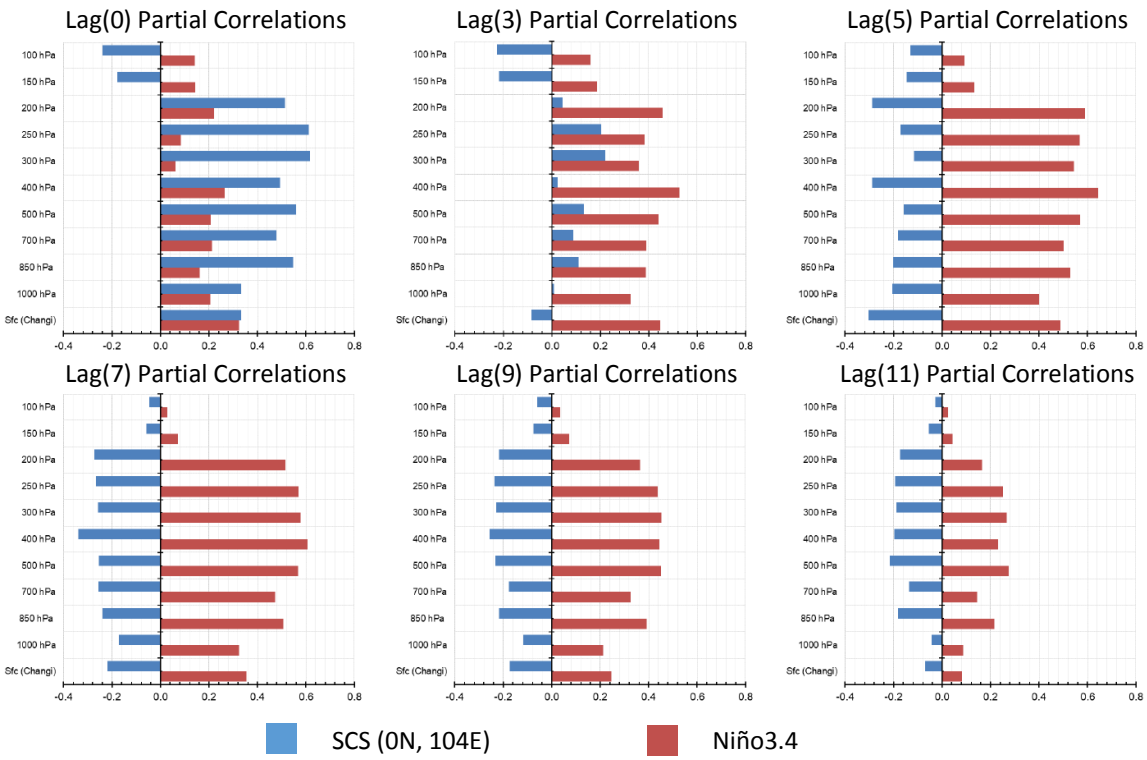

Figure 6 Partial correlations of the local air temperature at various levels with local (SCS, blue) and Niño3.4 (red) SST anomalies at different lags.

definition of El Niño years from June to May. It is noteworthy that at the surface, the remote relationship between Niño3.4 and Changi observed temperature is stronger than aloft and also stronger than with local SST. It suggests that an additional effect is captured; possibly the impact of ENSO on Singapore rainfall, since during an El Niño episode Singapore's climate tends to be drier with clearer skies, possibly leading to an additional signature on the surface temperature (from stronger insolation) compared to the atmospheric column aloft. Finally, it is worth noting near the tropopause, the relationship between local SST and temperature reverses while the relationship with ENSO remains of the same magnitude.

To further understand how the interplay between the Singapore air temperature profile and local versus remote (Niño3.4) SST evolves, the partial cross-correlation coefficients using monthly anomalies were calculated at various lags (Figure 6). The monthly anomalies are obtained by first detrending and then subtracting the climatology from the respective monthly time series. The maximum positive lag correlations indicate that local tropospheric air temperatures lag behind Niño3.4 SSTs by 5 months with significant correlations apparent between 3 and 9 months' lag. The timing of the maximum correlations is consistent with previous studies (e.g. Chiang and Sobel, 2002; Sobel et al. 2002). By the peak lag, the vertical profile shows increasing correlation values with height up to 400 hPa, suggesting that ENSO's influence is largely communicated to Singapore via an 'atmospheric bridge' through changes in the local Hadley and Walker circulations (e.g. Schwendike et al. 2014). In contrast to the remote relationship, which demonstrates increasing strength with lag, the relationship with the local SST is strongest at lag 0 before rapidly diminishing and even reverses by lag 5. Note that the negative correlation values remain more or less steady up to lag 11 (i.e. the relationship approaches a "quasi-steady" state). The behaviour at lags larger than 3 is thus consistent with the relaxation time scale needed to reach radiative-convective equilibrium in the tropics (e.g. Cronin and Emanuel 2013). In order words, the influence of local SST on the tropospheric column is largely due to convection in the near term (fast stabilising process) while the effect of radiative cooling in the atmosphere dominates at longer time scales (slow de-stabilising process). Furthermore, it suggests that there is a lack of auto-correlation in the local SST when the remote influence of ENSO is removed.

CONCLUSION

Homogenisation of monthly mean, upper-air temperature data for Singapore on standard pressure levels has been presented. Using the new homogeneous dataset, the vertical structure of temperature trends over Singapore for the period 1979-2016 has been explored. Tropospheric warming and lower stratospheric cooling are seen in the homogenised data, as expected from the physical response to on-going global warming. However, the magnitudes of the decadal warming trends in the upper troposphere (400-200 hPa) are greatly reduced from the original data trends by at least 50%, while a slight increase in warming trends is seen for the 850-700 hPa levels. A stronger cooling trend is also now apparent in the lower stratosphere above 200 hPa.

The trend at the lower level with a larger warming at 1000 hPa than 850 hPa is indicative of a broad UHI effect in the lower part of the planetary boundary layer above Singapore, which has rapidly urbanised during this period. This is confirmed by the surface warming being even stronger than at 1000 hPa: 0.44°C/decade at Paya Lebar and 0.32°C/decade at the Changi Airport climate station. These 1000 hPa and surface warming trends are in contrast to local SSTs, which have been warming at a pace similar to the 850 hPa level, both being unaffected by the growing UHI effect. The land trends are due to a combination of the local response to background global warming and urbanisation. The difference in land warming rates may be due to different degrees of urbanisation and land use between the two sites. The 1000 hPa trend is more likely to display a spatial smoothing of the local urbanisation effect and may be seen as representative of the combination of global warming and a "spatial average" of the UHI growing effect.

The tropospheric column temperature relationship to ENSO (via Niño3.4 SSTs) is also explored. Partial correlation analysis shows that ENSO affects the entire depth of the troposphere although slightly less than the local SSTs when averaged over a full year (computed using the ENSO cycle from June to May). Peak lag correlations indicate that monthly temperatures over Singapore tend to lag behind Niño3.4 SSTs by 5 months, consistent with regional estimates made in earlier studies looking into the teleconnection response of tropospheric temperatures globally. This is in contrast to local SSTs where the relationship is strongest at lag 0 and quickly disappears (lag 3) before reversing by lag 5. These results further highlight the remote forcing effect of Niño3.4 SSTs on Singapore's air temperature through an atmospheric bridge. Further research is needed to determine the exact mechanisms by which ENSO (combined with its influence on local SSTs) affects local tropospheric temperatures.

ACKNOWLEDGEMENTS

The authors are grateful to Lawrence Coy, Global Modelling and Assimilation Office, Goddard Space Flight Center, NASA for kindly providing Figure 2.

REFERENCES

Baldwin, M.P., Gray, L.J., Dunkerton, T.J., Hamilton, L., Haynes, P.H., Randel, W.J., Holton, J.R., Alexander, M.J., Hirota, I., Horinouchi, T., et al. (2001) The quasi-biennial oscillation. *Reviews of Geophysics*, 39: 179–229.

Chiang, J.C.H., Sobel, A.H. (2002) Tropical Tropospheric Temperature Variations Caused by ENSO and Their Influence on the Remote Tropical Climate. *Journal of Climate*, 15:2616–2631.

Christy, J.R., Spencer, R.W., Norris, W.B. (2011) The role of remote sensing in monitoring global bulk tropospheric temperatures. *International Journal of Remote Sensing*, 32:671–685.

Cronin, T. W., Emanuel, K. A. (2013) The climate time scale in the approach to radiative-convective equilibrium. *Journal of Advances in Modeling Earth Systems*, 5:843—849.

Dee, D.P., Uppala, S.M., Simmons, J., Berrisford P., Poli, P., Kobayahsi S., Andrae, U., Balmaseda, M.A., Balsamo, G., Bauer, P. et al. (2011) The ERA-Interim Re-Analysis: Configuration and performance of the data assimilation system. *Quarterly Journal of the Royal Meteorological Society*, 137:553–597.

Haimberger, L., Tavolato, C., Sperka, S. (2008) Toward Elimination of the Warm Bias in Historic Radiosonde Temperature Records — Some New Results from a Comprehensive Intercomparison of Upper-Air Data. *Journal of Climate*, 21:4587–4606.

Haimberger, L., Tavolato, C., Sperka, S. (2012) Homogenization of the global radiosonde temperature dataset through combined comparison with reanalysis background series and neighboring stations. *Journal of Climate*, 25:8108–8131.

Hassim, M.E.E., Timbal, B. (2019) Observed Rainfall Trends over Singapore and the Maritime Continent from the Perspective of Regional-Scale Weather Regimes.

Journal of Applied Meteorology and Climatology, 58: 365–384.

Huang, B., Thorne P.W., Banzon V.F., Boyer T., Chepurin G., Lawrimore J.H., Menne M.J., Smith T.M., Vose R.S., Zhang H.M. (2017) Extended reconstructed Sea surface temperature, Version 5 (ERSSTv5): Upgrades, validations, and intercomparisons. *Journal of Climate*, 30:8179–8205.

Jovanovic, B., Smalley, R., Timbal, B., Siems, S. (2017 Homogenized monthly upper-air temperature data set for Australia. *International Journal of Climatology*, 37:3209–3222.

Madden, R. A., Julian, P.R. (1972) Description of Global-Scale Circulation Cells in the Tropics with a 40–50 Day Period. *Journal of Atmospheric Sciences*, 29:1109–1123.

Maruyama, T. (1991) Annual and QBO-Synchronized Variations of Lower-Stratospheric Equatorial Wave Activity over Singapore during 1961-1989. *Journal of the Meteorological Society of Japan*. Ser. II, 69:219–232.

Mears, C.A., Wentz, F.J. (2009a) Construction of the Remote Sensing Systems V3.2 Atmospheric Temperature Records from the MSU and AMSU Microwave Sounders. *Journal of Atmospheric and Oceanic Technology*, 26:1040–1056.

Mears, C.A., Wentz, F.J. (2009b) Construction of the RSS V3.2 Lower-Tropospheric Temperature Dataset from the MSU and AMSU Microwave Sounders. *Journal of Atmospheric and Oceanic Technology*, 26:1493–1509.

Schwendike, J., Govekar, P., Reeder, M.J., Wardle, R., Berry, G.J., Jakob, C. (2014) Local partitioning of the overturning circulation in the tropics and the connection to the Hadley and Walker circulations. *Journal of Geophysical Research: Atmospheres*, 119:1322–1339.

Sherwood, S.C., Nishant, N. (2015) Atmospheric changes through 2012 as shown by iteratively homogenized radiosonde temperature and wind data (IUKv2). *Environmental Research Letters*, 10:054007.

Sobel, A.H., Held, I.M., Bretherton, C.S. (2002) The ENSO Signal in Tropical Tropospheric Temperature. *Journal of Climate*, 15:2702–2706.

Trenberth, K.E., Caron, J.M., Stepaniak, D.P., Worley, S. (2002) Evolution of El Niño–Southern Oscillation and global atmospheric surface temperatures. *Journal of Geophysical Research,* 107:4065.

Wang, X., Feng, Y. (2007) RHTestV3 User Manual. Climate Research Division, Environment Canada, Toronto, Canada.

Wang, X.L. (2008a) Accounting for Autocorrelation in Detecting Mean Shifts in Climate Data Series Using the Penalized Maximal t or F Test. *Journal of Applied Meteorology and Climatology*, 47:2423–2444.

Wang, X.L. (2008b) Penalized Maximal F Test for Detecting Undocumented Mean Shift without Trend Change. *Journal of Atmospheric and Oceanic Technology* 25:368–384.

Wang, X.L., Wen, Q.H., Wu, Y. (2007) Penalized Maximal t Test for Detecting Undocumented Mean Change in Climate Data Series. *Journal of Applied Meteorology and Climatology*, 46:916–931.

Yulaeva, E., Wallace, J.M. (1994) The Signature of ENSO in Global Temperature and Precipitation Fields Derived from the Microwave Sounding Unit. *Journal of Climate*, 7:1719-1736.

STRUCTURES OF THE BACKGROUND ERROR COVARIANCE MATRIX FOR SINGV

Joshua Lee and Xiang-Yu Huang

Weather Modelling and Development Section, Centre for Climate Research Singapore, Meteorological Service Singapore

INTRODUCTION

Data assimilation seeks to combine the information from observations with prior information from a system through a mathematically optimal approach. The aim is to get the best estimate of the state of the system. For numerical weather prediction (NWP), it is impossible to know the full state of the system at every gridpoint. To best estimate the full state, a short-range forecast cannot be used alone because it may not be accurate. However, observations cannot be used alone as well because we neither observe every model variable nor have observations at every gridpoint. Both approaches can be complementary; a short-range forecast can be used to guess the full state of the system, and weather observations can be used to make small corrections to that guess. Many assumptions and complexities are involved to optimise the use of both information in what is called 'data assimilation'. Various data assimilation methods have been developed, each with its own limitations and applicability. These include variational methods, Kalman filters, and particle filters. At the Meteorological Service Singapore (MSS), the variational data assimilation method is used operationally in a tropical convective-scale NWP system (SINGV).

The variational data assimilation method solves the optimisation problem by combining information from observations and information from a short-range forecast weighted by their uncertainties. The short-range forecast (guess) contains background information retained by the model from previous cycles; it is often called the background. There are errors in the background and observations, closely linked to their uncertainties. If the background errors are large relative to observation errors, more weight is given to information from observations and larger corrections are made to the guess. Specifying the errors for every variable and gridpoint in the background (and their covariances) and every observation (and their covariances) results in the background error covariance matrix and observation error covariance matrix respectively. The observation error covariance matrix does not vary substantially because the observation errors are relatively consistent in different NWP systems. However, the background error covariance matrix depends heavily on the forecast model setup, so it differs in various NWP systems and requires proper specification and tuning. Despite this, the large background error covariance matrix (~10^{14} elements) is computationally unfeasible to specify explicitly. More importantly, it is impossible to know the true state, and hence background errors, of the NWP system. Thus, the background error covariance matrix is also analytically impossible to specify explicitly; it must be estimated and modelled (Bannister 2008a).

In addition to its role in weighting information from the background and observations, the background error covariance matrix also determines the spreading of information from observations. Errors in observations are typically assumed to be uncorrelated with each other; the correlation of information between gridpoints and variables are captured by the "off-diagonals" of the background error covariance matrix. The modelled background error covariance matrix is complex, but can be understood in terms of the horizontal and vertical structure functions it comprises. These structure functions determine the spreading of information from observations, through corrections to the guess for nearby horizontal and vertical gridpoints. Due to non-zero error covariances between variables, information from observations of one model variable also produces corrections to the guess for other model variables. Ideally, these corrections should be dynamically consistent. To illustrate, it would be plausible to perform cyclonic wind corrections based on a high pressure observation near the surface which corresponds to geostrophic balance in the mid-latitudes.

These structure functions are statistically modelled, and estimated from training data based on the assumptions of homogeneity, isotropy and time-averaging, so their sensitivity to different training data needs to be understood. The same climatological (time-

averaged) structure functions are often used for each assimilation cycle, regardless of the varying flow conditions from different weather phenomena occurring in reality. Consequently, they may be dynamically inconsistent with the flow. For example, the corrections to the guess required for a mesoscale convective system may be different to that for a frontal system. Different training data will result in different error statistics (and possibly structure functions). Thus, the fine-tuning would help to identify characteristics of the training data which result in modelled structure functions that are dynamically consistent for most flow conditions in the NWP system. Some of the most advanced assimilation systems include a flow-dependent estimation of the background error statistics (e.g. the system used at the European Centre for Medium-Range Weather Forecasts; Bonavita et al. 2011).

In this paper, we provide a brief mathematical justification and theoretical framework for modelling the background error covariance matrix for SINGV and evaluating its structure functions. Nine background error covariance matrices are generated from different training data. The sensitivity of their modelled structure functions to different training data are analysed using pseudo-single observations experiments and compared to the background error covariance matrix presently used in the Singapore Parallel Suite 2 (SPS2) configuration (referred to as oldDS; provided by the Met Office in 2015). Their individual performance in a week-long data assimilation trial with real observations is also assessed.

VARIATIONAL DATA ASSIMILATION THEORETICAL FRAMEWORK

The theoretical framework for variational data assimilation is underpinned by Bayes' theorem: the best estimate of the state can be found from the conditional probability of the state given the observations (posterior). This is mathematically a function of the probability of the state (prior) and conditional probability of the observations occurring given the state (likelihood). The best estimate of the state is known as the analysis. The variational approach involves finding the analysis that minimises a cost function. Here, we present a brief mathematical discussion. The full mathematical derivation can be found in Kalnay (2003). Assuming that the prior and likelihood follow a Gaussian probability distribution, we apply Bayes' theorem to determine the posterior. We formulate an expression for the cost function, also known as the penalty or objective function, given by:

$$J(\mathbf{x}) = J_b(\mathbf{x}, \mathbf{x_b}, \mathbf{B}) + J_o(\mathbf{x}, \mathbf{y}, \mathbf{R}) \quad (1)$$

where J_b is the penalty contribution by the model, $\mathbf{x}$ is the 3-dimensional state of variables, $\mathbf{x_b}$ is a prior estimate of the state (background), $\mathbf{B}$ is the background error covariance matrix which we model, J_o is the penalty contribution by observations, $\mathbf{y}$ is the observations vector and $\mathbf{R}$ is the observation error covariance matrix. From Equation 1, J_b is larger if $\mathbf{x}$ deviates more from $\mathbf{x_b}$ with smaller background errors. J_o is larger if $\mathbf{x}$ deviates more from its corresponding observations with smaller observation errors. The analysis ($\mathbf{x} = \mathbf{x_a}$) that minimises this cost function has the maximum *a posteriori* probability; it is the mode of the posterior.

The solution $\mathbf{x_a}$ (see Kalnay 2003 for simplifications and proof) is the Best Linear Unbiased Estimator, given by:

$$\mathbf{x_a} = \mathbf{x_b} + \mathbf{K}(\mathbf{B}, \mathbf{R})\mathbf{d}(\mathbf{x_b}, \mathbf{y}) \quad (2)$$

where $\mathbf{K}$ is commonly referred to as the gain matrix, as a function of $\mathbf{B}$ and $\mathbf{R}$. $\mathbf{d}$ is the difference between observations and the equivalent observations constructed from the background (background mapped to observation space); called the innovation, as a function of $\mathbf{x_b}$ and $\mathbf{y}$. This important result quantitatively estimates the corrections ($\mathbf{Kd}$) to add to the background, hereafter referred to as increments (denoted by superscript primes e.g. p'). This is the mathematically optimal approach for finding the best estimate of the state in variational data assimilation.

MODELLING THE **B** MATRIX FOR SINGV

Several studies have documented various methods to model $\mathbf{B}$ for an NWP system (Derber and Bouttier 1999; Jackson et al. 2008; Bannister 2008b, Bonavita et al. 2011; Massart 2018). One of the methods is the "National Meteorological Center (NMC)" method (Parrish and Derber 1992), which is based on estimating $\mathbf{B}$ using difference between pairs of forecasts of different lengths which are valid at the same time. Mathematically, this is derived in Bannister (2008a). The training data comprise these pairs of forecasts. All the training data are generated from the SINGV 5.0 downscaler (SINGV-DS) run at 4.5 km horizontal resolution, driven by global European Centre for Medium-Range Weather Forecasts (ECMWF) analyses and forecasts. $\mathbf{B}$ can then be modelled from the various training data.

The modelling process involves a control variable transform, a vertical transform and a horizontal transform. We apply the transforms in this specific order (see Appendix A for more details). The mathematical details are covered in Bannister (2008b). Default options are used, regarding: (1) the configuration of the humidity control variable and associated binning options, (2) configuration of the velocity potential control variable, and (3) variance binning options. These options are not discussed in detail.

In this work, we focus mainly on investigating the sensitivity of the structure functions of $\mathbf{B}$ to:

- The training data period;
- The difference in forecast length for pairs of forecasts.

Table 1 Details of the training data generated using SINGV-DS. The nine background error covariances are modelled according to training data period (columns) and difference in forecast length of pairs of forecasts (rows). The number of pairs of forecasts used (sample size) and the abbreviation of their modelled covariance matrix are indicated in each cell. oldDS is also shown, although its details are not documented.

SINGV-DS training data details	February 2018	May 2018	September 2018
3H difference in forecast length (6-3H)	Sample size: 56 Abbreviation: FEB6-3H	Sample size: 62 Abbreviation: MAY6-3H	Sample size: 58 Abbreviation: SEP6-3H
6H difference in forecast length (12-6H)	Sample size: 56 Abbreviation: FEB12-6H	Sample size: 62 Abbreviation: MAY12-6H	Sample size: 58 Abbreviation: SEP12-6H
12H difference in forecast length (24-12H)	Sample size: 28 Abbreviation: FEB24-12H	Sample size: 31 Abbreviation: MAY24-12H	Sample size: 29 Abbreviation: SEP24-12H

oldDS 6H difference in forecast length (12-6H)	Training data period: 22/01/13 to 06/03/13

The details of the training data are presented in Table 1. The months for the training data periods are chosen to correspond to the end of the Northeast Monsoon (February) and Southwest Monsoon (September). Additionally, May is included since the data assimilation trials are performed during that period. It would be useful to investigate if the structure functions are more dynamically consistent when the input $\mathbf{B}$ is modelled from the same training data period as the data assimilation trial.

There are many possible combinations of forecast pairs with the same validity time, which can be used to compute differences. For example, 22-10H (the difference between a 22-hour forecast, and a 10-hour forecast issued 12-hours after, and thus both valid at the same time) gives the same desired difference in forecast length of 12 hours as 24-12H. It is not necessary to strictly adhere to the choice of combinations (Bannister 2008a). We choose the difference in forecast length such that the pairs of forecasts use the same lateral boundary conditions (LBCs) for each period, as required by the lagged NMC method.

PSEUDO-SINGLE OBSERVATION EXPERIMENTS

Equation 2 is important for understanding the use of pseudo-single observation experiments. A pseudo-single observation would only have one element in $\mathbf{R}$ (the error it is associated with) and one non-zero element in $\mathbf{d}$ (see Derber and Bouttier 1999 for full equation). Assuming these are constant, the multivariate structure functions of $\mathbf{B}$ would be extracted and be directly related to the increments. The sensitivity of the structure functions to different training data can then be analysed.

A pseudo-single observation of pressure (p) is inserted near the centre of the model domain at model level 15 (~1 km height) [suite u-bb581]. An innovation ($\mathbf{d}$) of 100 Pa (1 hPa) is specified. We specify the observation error to be 20 Pa (0.2 hPa), which is sufficiently large so that some information from the background will be used to find the analysis; the increments will be sensitive to $\mathbf{B}$.

From the pseudo-single observation experiments, the structure functions of different $\mathbf{B}$ at model level 15 are extracted (Figure 1). They indicate how p errors of the modelled $\mathbf{B}$ are correlated spatially. This correlation structure function determines how an observation of p at a point influences the p field in the domain, which is updated accordingly by p'. Note also that p' from multiple observations can be accumulated. These are extremely important for a data-sparse region like the tropics. Figure 1 shows that p' decreases non-

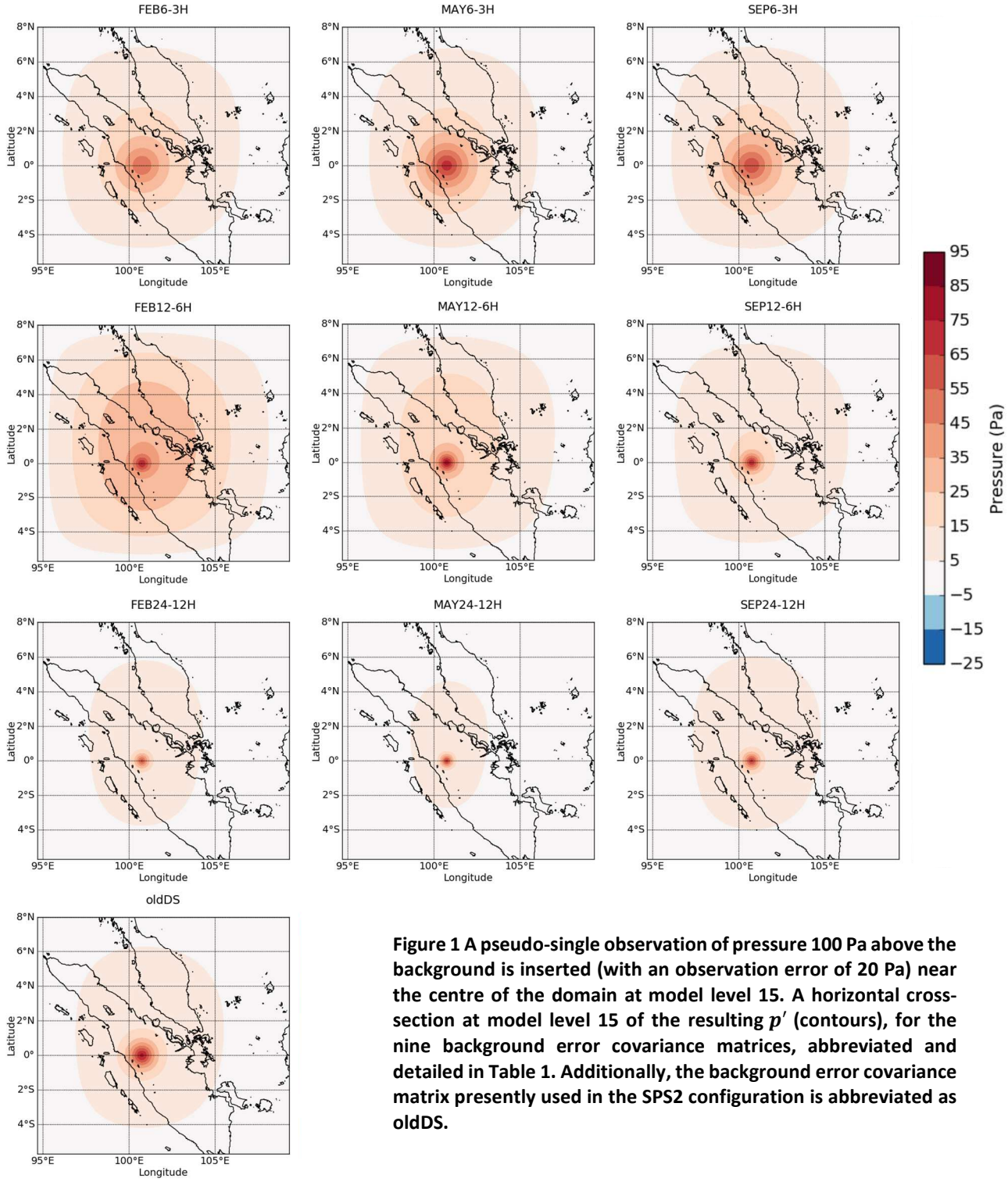

Figure 1 A pseudo-single observation of pressure 100 Pa above the background is inserted (with an observation error of 20 Pa) near the centre of the domain at model level 15. A horizontal cross-section at model level 15 of the resulting p' (contours), for the nine background error covariance matrices, abbreviated and detailed in Table 1. Additionally, the background error covariance matrix presently used in the SPS2 configuration is abbreviated as oldDS.

linearly and near-isotropically from the point of observation. The extent of the decrease is governed mainly by the horizontal structure functions (horizontal length-scales).

We first compare the sensitivity of the horizontal structure functions to the difference in forecast length. In general, the horizontal length-scales are longest for 6-3H covariances. This implies that p' is spread by the error correlations throughout almost the whole domain. By contrast, the horizontal length-scales are shortest for 24-12H covariances. Correspondingly, p' is more localised. For 12-6H covariances, p' is also concentrated over a small region, although there are small increments which extend throughout the domain. This is similarly observed for the oldDS covariance (a 12-6H covariance). The SEP12-6H covariance most closely resembles the oldDS covariance. It is interesting to note that larger difference in forecast length resulted in shorter horizontal length-scales. To our knowledge, no paper has previously reported this in the tropics. Ingleby (2001) suggested that horizontal length-scales may tend to increase as length of forecast increases due to errors

on synoptic scales. However, there is no empirical evidence for this. In practice, we may instead be concerned with errors on convective scales. It is also possible that the horizontal-length-scales are overestimated for small differences in forecast length (e.g. 6-3H).

Next, the results are compared between training data periods (columns). We observe that there is no distinct pattern. This suggests that the horizontal structure functions of p are more sensitive to the difference in forecast length than training data period. As there have been very few studies on pseudo-single observation experiment results in the tropics, it is difficult to determine whether the longer horizontal length-scales in 6-3H covariances are desirable. Ingleby (2001) found that the horizontal length-scales associated with forecast error statistics were longer in the tropics than mid-latitudes. Žagar et al. (2004) found that wind field observations in the tropics recovered finer horizontal structure functions of geopotential height field (associated with p), which was deemed as desirable. Ideally, the structure functions of $\mathbf{B}$ (and hence increments) should be dynamically consistent with adjustment or balanced processes. However, tropical convective-scale data assimilation is tricky, without a unified theoretical framework, and many processes could be responsible for their structure functions.

Also, from the maximum of p' at the point of observation, we can rearrange Equation 2 to compute the domain-averaged background error standard deviations (an element in $\mathbf{B}$; σ_p). We test the sensitivity of the background error standard deviations to difference in forecast length, listed in Table 2. σ_p, (and hence p'), is slightly larger for 12-6H covariances compared to the other covariances. The reason is not clear, although it could be related to the validity times of the 12-6H training data and the diurnal cycle. Alternatively, low values for 24-12H could simply be because of a smaller sample size, so there may be less variation. It is also interesting to observe that regardless of the difference in forecast length, σ_p is slightly larger in May (Table 2).

Table 2 Background error standard deviations of pressure for the nine background error covariance matrices, according to training data period (columns) and difference in forecast length (rows). oldDS is also shown for comparison.

σ_p (Pa)	FEB	MAY	SEP
6-3H	21.8	30.9	26.5
12-6H	35.1	42.5	32.6
24-12H	23.9	29.2	28.7

oldDS	37.0

Larger domain-averaged background error standard deviations suggest that the model is more uncertain, indicating that we might be more inclined to give more weight to observations during the data assimilation process, with correspondingly larger increments. It is difficult to determine if larger increments are desirable; they may result in larger initialisation shocks to the model field, leading to enhanced excitation of spurious gravity waves. By contrast, smaller increments may erroneously suggest that information from the background is more reliable than information from observations.

Figure 2 shows a comparison between the vertical structure functions of different $\mathbf{B}$, using a vertical cross-section at the latitude of observation. The first 70 model levels are shown (instead of all 80 levels) to focus on the vertical structure functions in the troposphere and stratosphere. There is an anti-correlation between p' in the lower troposphere (model levels ~10–25) and upper troposphere (model levels ~40–60). This is observed for all nine background error covariances, albeit with different anti-correlation magnitudes.

We investigate the sensitivity of the vertical correlation structure functions to difference in forecast length. There is little variation other than in the horizontal correlations at different levels. Vertically, p' extends up to around model level 30 (~4.3 km height), and the anti-correlation of p' is confined to model levels 40–60 for all cases, appearing slightly weaker for 24-12H covariances. There is even less variation when comparing between training data periods, most of the variation is related to the magnitude of p'. The SEP12-6H covariance is again most similar to the oldDS covariance. The results suggest that vertical structure functions of p are not sensitive to both training data period and the difference in forecast length. These robust structure functions may not correspond to balance or adjustment processes, so this needs further investigation to ensure dynamical consistency.

Apart from the spreading of information spatially, there are structure functions of $\mathbf{B}$ that spread information between fields through modelled correlations. We first consider the mass-wind coupling captured by $\mathbf{B}$. Figure 3 shows a comparison of the pressure-wind horizontal structure functions of the different $\mathbf{B}$. We note that these structure functions may be indicative of complex contributions from equatorial

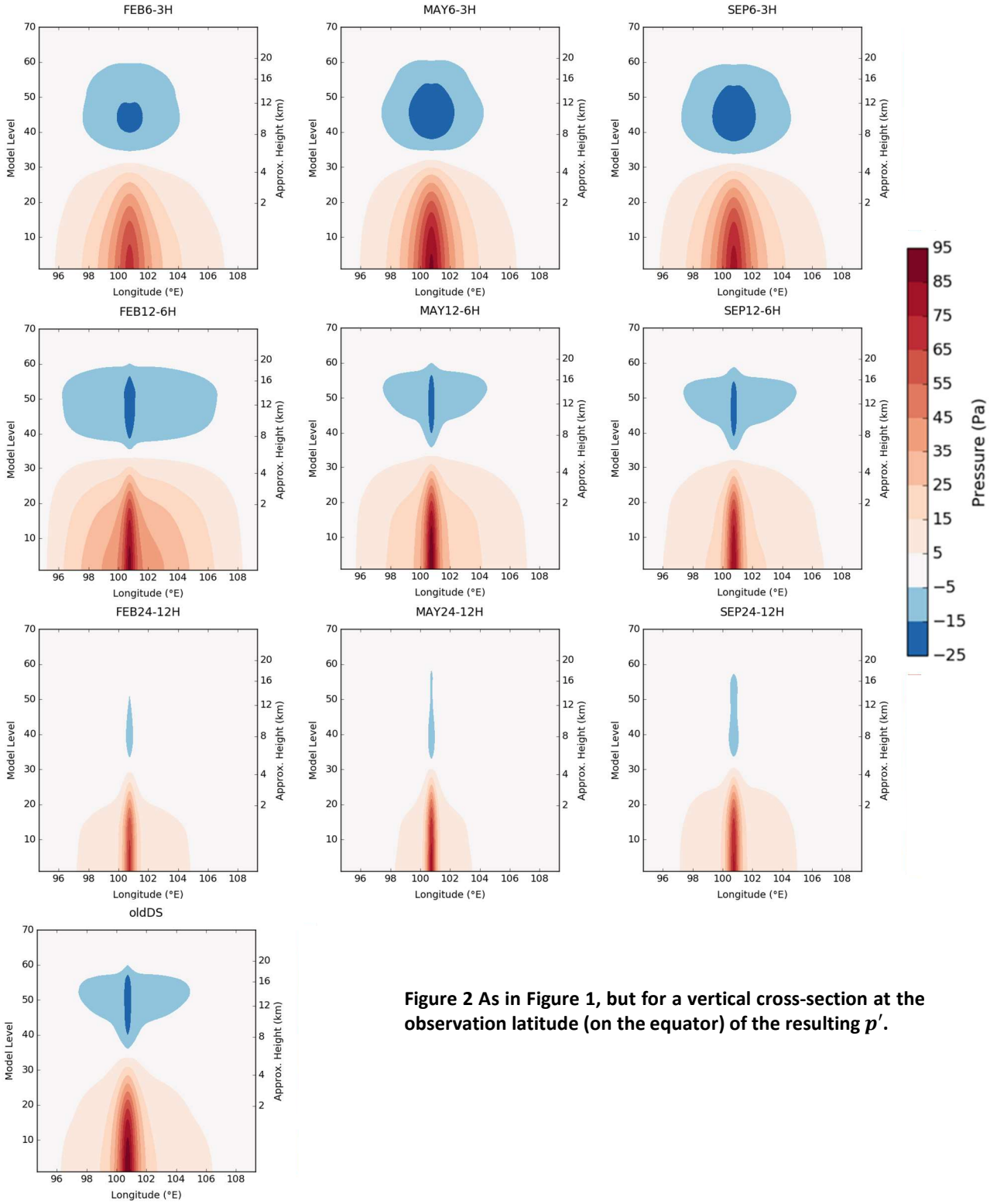

Figure 2 As in Figure 1, but for a vertical cross-section at the observation latitude (on the equator) of the resulting p'.

Rossby waves, Kelvin waves, mixed Rossby gravity waves, and equatorial inertia-gravity waves (Žagar et al. 2004). Comparing between the difference in forecast length, there is substantial variation; the mass-wind coupling is weak for 6-3H and 24-12H covariances. Comparing between training data periods, there is little variation; a similar mass-wind coupling pattern is observed regardless of difference in forecast length.

The results show how the mass-wind coupling captured by $\mathbf{B}$ is dependent on the difference in forecast length. 12-6H covariances capture the structure of a Kelvin wave with westerly wind increments (positive correlations) at the point of observation, similar to Figure 6a of Žagar et al. (2004). This structure function is likely dominated by contributions from Kelvin and equatorial inertia-gravity waves. By contrast, the weak easterly wind increments for 24-12H and 6-3H covariances are indicative that the structure function is dominated by contributions from the lowest equatorial Rossby mode, related to negative

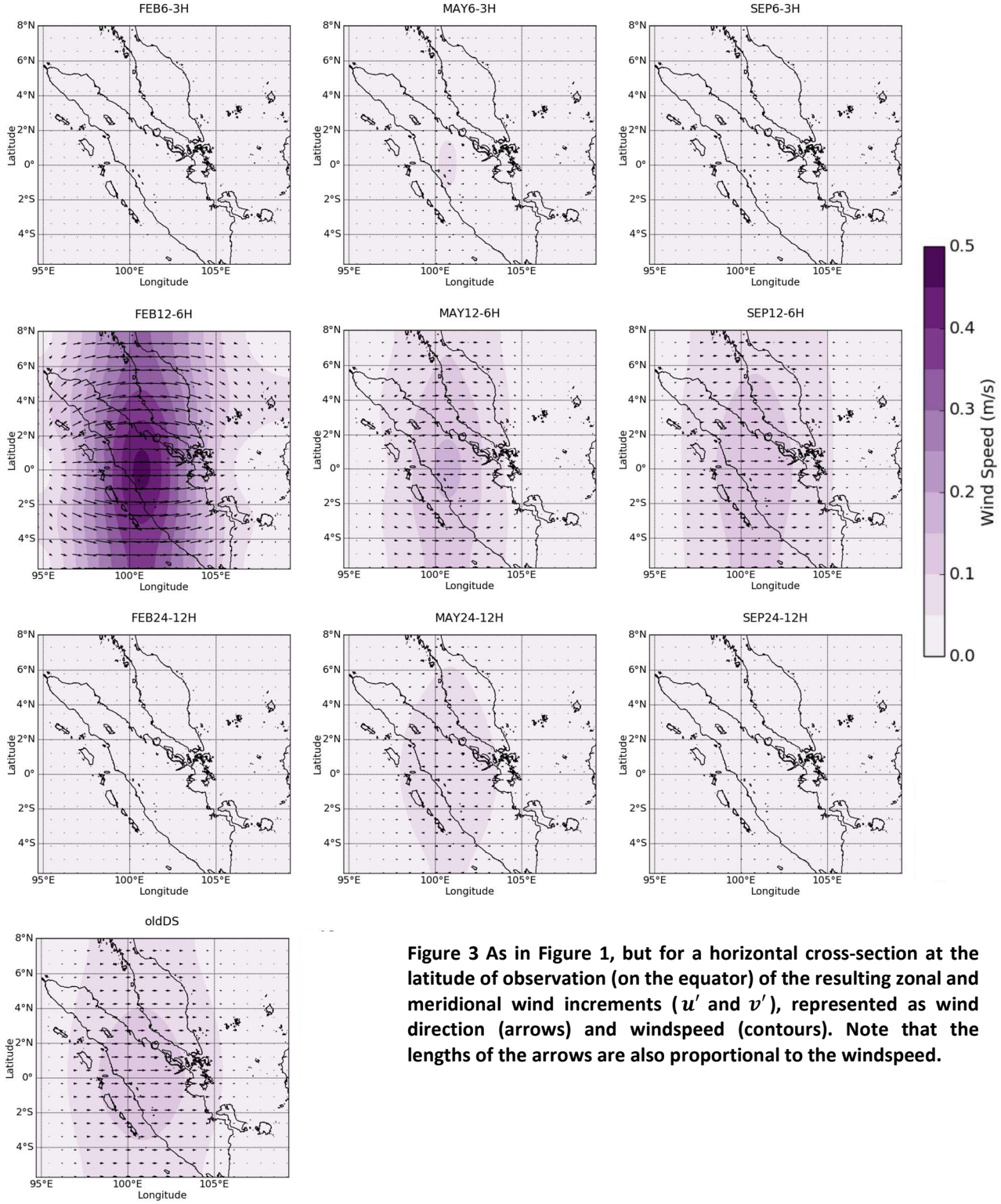

Figure 3 As in Figure 1, but for a horizontal cross-section at the latitude of observation (on the equator) of the resulting zonal and meridional wind increments (u' and v'), represented as wind direction (arrows) and windspeed (contours). Note that the lengths of the arrows are also proportional to the windspeed.

correlations between p' and u' (see Figure 3a of Žagar et al. 2004; Figure 5c of Daley 1993). While these structure functions are modelled from forecast errors rather than actual fields, it may be useful to analyse their dynamical consistency during the passage of different equatorial waves (or flow conditions). Interestingly, the pressure-wind vertical structure functions (not shown) also reveal regions of convergence and ascent downwind of the observation. The opposite occurs upwind of the observation. This requires further investigation.

Next, we consider the mass-moisture coupling captured by $\mathbf{B}$. Figure 4 shows a comparison of the pressure-moisture vertical structure functions of the different $\mathbf{B}$. q' is largely a function of p', so their horizontal extent of correlations are similar (not shown). Vertically, q' is noticeably patchy, due to the complexity of the transforms associated with multiple model variables. The results show that p' and q' are

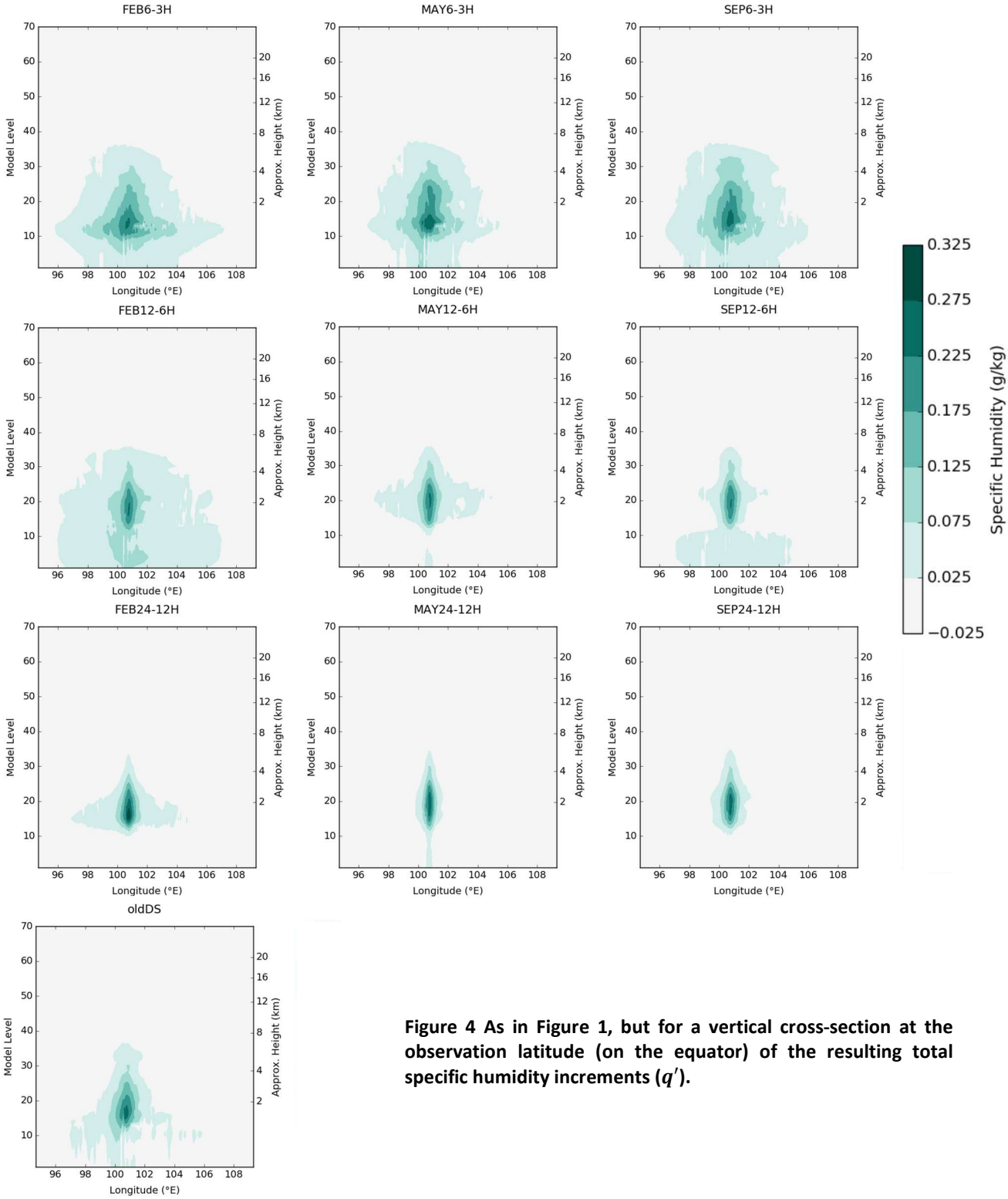

Figure 4 As in Figure 1, but for a vertical cross-section at the observation latitude (on the equator) of the resulting total specific humidity increments (q').

generally positively correlated, confined to a small range of model levels. Also, a comparison between the difference in forecast length and training data periods both show little variation. Considering the availability of moisture (~18 g/kg) in the deep tropics, these increments are small. However, the small moisture increments could become important when they are accumulated from multiple observations.

DATA ASSIMILATION TRIALS

To assess the impact of using different $\mathbf{B}$, data assimilation trials are performed using real observations from the period 20180429T0300Z to 20180508T2100Z. The SPS2 configuration is used, except that oldDS is replaced. The model's 3-hour forecasts fit to observations (referred to as observation minus background; O-B) is used as a metric for assessing the performance of each $\mathbf{B}$ compared to the oldDS. O-B statistics for radiosonde relative humidity, temperature, zonal wind and meridional wind; surface temperature

and relative humidity; aircraft temperature, zonal wind and meridional wind are calculated, averaged over all cycles where observations are available within the period. Additionally, O-B statistics are averaged vertically for radiosonde variables.

Figure 5 shows a comparison between the nine background error covariances compared to oldDS. A negative value in percentage change in the cycle-averaged O-B root-mean-square (RMS) difference indicates that the model's 3-hour forecast tends to have a closer fit to observations, which is desirable assuming that observations are accurate.

We compare the results first between the difference in forecast length. The results show that the 6-3H covariances perform substantially poorer than the oldDS (Figure 5a); there are larger cycle-averaged O-B RMS, in almost all the variables assessed. This indicates poorer overall fit in the model atmospheric profile to observations. This could be due to many reasons, one of which could be due to the large horizontal length-scales generally seen in the 6-3H covariances. Following that argument, the 24-12H covariances perform slightly better than the oldDS (Figure 5c). This could possibly be related to more localised spreading of information from observations. It could also be related to the weaker anti-correlation in their vertical structure functions which may be desirable. The oldDS only gives better fit for surface variables. Additionally, 12-6H covariances performed only marginally worse than 24-12H covariances, which could be related to the larger increments discussed earlier.

We also compare the results between training data periods. There are little distinguishing features. Different covariances perform better for different variables. More notably, May covariances did not exhibit improved O-B fits even though the data assimilation trial was also performed in May. This suggests that the dynamical consistency of the structure functions of $\mathbf{B}$ for SINGV is not improved even when it is modelled from the same training data period as the trial. It is possible that the seasonal dependence of $\mathbf{B}$ may not be important in SINGV. We note that the strong mass-wind coupling in 12-6H covariances also did not distinctly result in better O-B fits.

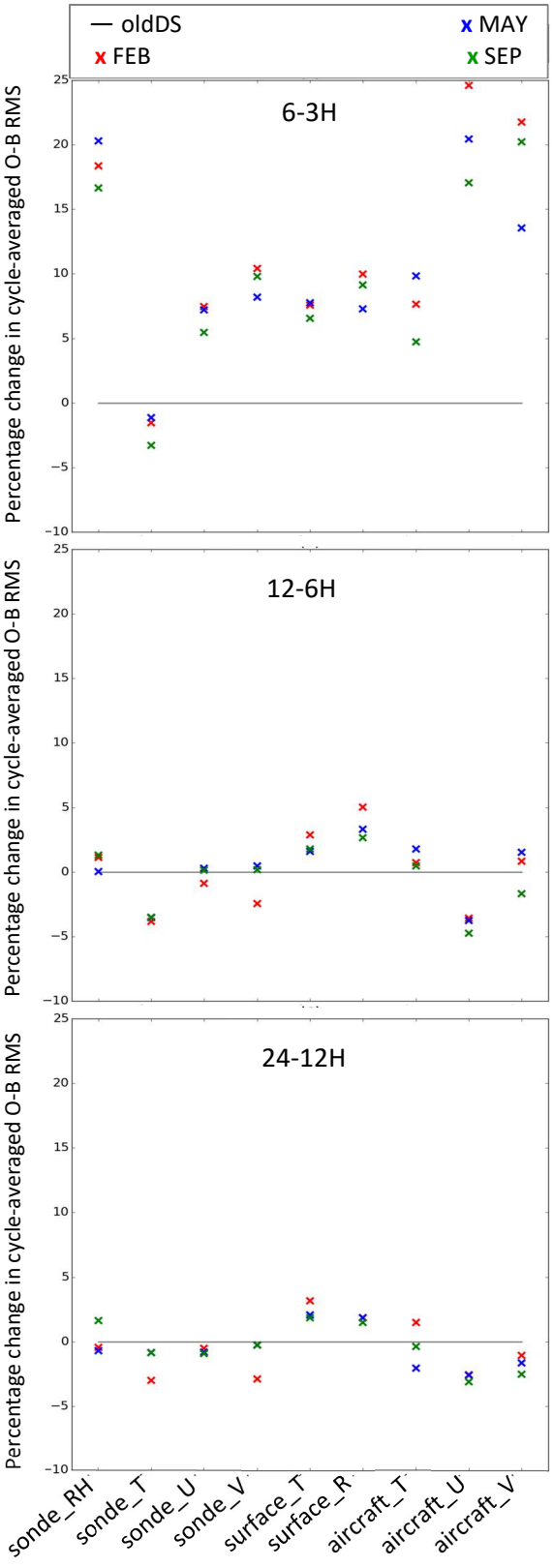

Figure 5 Percentage change in cycle-averaged O-B RMS for radiosonde relative humidity, temperature, zonal wind and meridional wind (sonde_RH, T, U, V); surface temperature, relative humidity (surface_T, RH); aircraft temperature, zonal and meridional wind (aircraft_T, U, V) for the nine background error covariances compared to oldDS from data assimilation trials. Top to bottom plots show the 6-3H, 12-6H and 24-12H covariances, respectively, abbreviated and detailed in Table 1.

DISCUSSION

A practical approach is taken for this paper, aimed at tuning $\mathbf{B}$ for SINGV. It is also aimed at providing a general introduction of the theoretical framework for colleagues who are unfamiliar with data assimilation. As such, the validity of the dynamical

concepts which underpins the mapping of model variables to control variables are not covered. The focus has mainly been on the structure functions related to p, but any improvements or degradation in O-B fits could be due to structure functions related to other variables as well. This can be complex to evaluate in tropical convective-scale data assimilation.

We note that other factors could have influenced the results. Model spin-up in the training data could have affected the 6-3H (and even 12-6H) covariances; this further indicates that larger differences in forecast length may be desirable, as shown in this paper. It would be useful to run data assimilation trials for a longer period to get better statistics of the O-B fits, although this is time-consuming.

While some of the new background error covariances (e.g. 24-12H covariances) have only shown slight improvements in O-B fits compared to oldDS, it is shown that poorer O-B fits can also be exhibited if $\mathbf{B}$ is not tuned properly (e.g. 6-3H covariances). There may be potential for exploring sensitivities of the structure functions of $\mathbf{B}$ to other criteria, such as transform order and forecast model resolution. It is also hoped that information about the uncertainty of the background can be gained from a parallel ensemble run. It would be useful to combine error statistics from the ensemble run and the modelled $\mathbf{B}$ in hybrid variational-ensemble data assimilation to improve the dynamical consistency of $\mathbf{B}$ in different flow conditions (accounting for flow dependency).

The tuning of $\mathbf{B}$ is unique to every NWP system. The current operational SINGV setup uses preliminary oldDS which Met Office modelled. Further assessment and tuning of $\mathbf{B}$ is required, understood from a dynamical perspective and not only by "trial-and-error".

CONCLUSION

This paper aimed at providing a general introduction to data assimilation, and to the impact of using different background error covariances. Attention has been placed on the tropical convective-scale NWP system operational at MSS, SINGV. From a practical perspective, the tuning of the background error covariances requires in-depth dynamical understanding of the underlying multivariate structure functions, which arise from the input training data used to model it.

We computed nine background error covariances and investigated the sensitivity of the structure functions of the background error covariance matrix to the training data period and the difference in forecast length of pairs of forecasts. Pseudo-single observation experiments were used to extract the multivariate structure functions. The background error covariance matrices were then tested in week-long data assimilation trials with real observations to assess their dynamical consistency in varying flow conditions.

We found that the horizontal structure functions of pressure in the background error covariances were more sensitive to difference in forecast length than training data period. The results show that a more localised spreading of observational information from larger differences in forecast length may be desirable. Robust vertical structure functions of pressure in the background error covariance matrices were also found to be somewhat insensitive to both training data period and difference in forecast length. These are indicative of balance or adjustment processes that are captured in the background error covariance matrix, which need to be further investigated to ensure dynamical consistency.

Mass-wind coupling and mass-moisture coupling was shown to be more sensitive to the difference in forecast length than training data period. While the mass-moisture coupling did not vary, the mass-wind coupling showed substantial variation related to contributions from different equatorial waves. These structure functions also need to be dynamically understood, so that their validity in a tropical convective-scale framework can be assessed.

The data assimilation trial results were sensitive to the difference in forecast length but suggested no seasonal dependence. Some of the new background error covariances showed slight improvements in O-B fits compared to the current operational SINGV background error covariance. Others showed substantially poorer O-B fits. There may be potential for further tuning of the background error covariance matrix for SINGV.

ACKNOWLEDGEMENTS

We thank our colleagues Anurag Dipankar, Peter Heng and Jerry Liu for providing helpful suggestions and inputs on both technical issues and the results. We also thank the Met Office staff for supporting MSS in the partnership.

REFERENCES

Bannister, R.N. (2008a) A review of forecast error covariance statistics in atmospheric variational data assimilation. I: Characteristics and measurements of

forecast error covariances. *Quarterly Journal of the Royal Meteorological Society*, 134:1951–1970.

Bannister, R.N. (2008b) A review of forecast error covariance statistics in atmospheric variational data assimilation. II: Modelling the forecast error covariance statistics. *Quarterly Journal of the Royal Meteorological Society*, 134:1971–1996.

Bonavita, M., Raynaud, L., Isaksen, L. (2011) Estimating background error variances with the ECMWF Ensemble of Data Assimilations system: some effects of ensemble size and day to day variability. *Quarterly Journal of the Royal Meteorological Society*, 137:423–434.

Daley, R. (1993) Atmospheric data assimilation on the equatorial beta plane. *Atmosphere-Ocean*, 31:421–450.

Derber, J., Bouttier, F. (1999) A reformulation of the background error covariance in the ECMWF global data assimilation system. *Tellus A: Dynamic Meteorology and Oceanography*, 51:195–221.

Ingleby, N.B. (2001) The statistical structure of forecast errors and its representation in The Met. Office Global 3-D Variational Data Assimilation Scheme. *Quarterly Journal of the Royal Meteorological Society*, 127:209–231.

Jackson, D.R., Keil, M., Devenish, B.J. (2008) Use of Canadian Quick covariances in the Met Office data assimilation system. *Quarterly Journal of the Royal Meteorological Society*, 134:1567–1582.

Kalnay, E. (2003) Atmospheric Modeling, Data Assimilation and Predictability. Cambridge University Press: Cambridge, UK.

Massart, S. (2018) A New Hybrid Formulation for the Background Error Covariance in the IFS: Implementation Aspects. European Centre for Medium Range Weather Forecasts. Available at: https://www.ecmwf.int/node/18747, last accessed 16 July 2019.

Parrish, D.F., Derber, J.C. (1992) The National Meteorological Center's spectral statistical-interpolation analysis system. *Monthly Weather Review*, 120:1747–1763.

Žagar, N., Gustafsson, N., Källén, E. (2004) Variational data assimilation in the tropics: The impact of a background-error constraint. *Quarterly Journal of the Royal Meteorological Society*, 130:103–125.

APPENDIX

The steps to model $\mathbf{B}$ [suite am-644] from the training data are outlined qualitatively here (also briefly in Met Office, 2013a). Technical details are in Met Office (2018).

The preliminary step involves taking the forecast difference for each pair of forecasts; performed on every element in the model forecast state (i.e. gridpoint-by-gridpoint, field-by-field). The sample mean (time-mean) is removed and the output fields are referred to as $\mathbf{e}$ (variables are denoted by a subscript *e*; strictly speaking these are approximations to the forecast errors, sometimes confusingly termed as increments).

The next step involves a mapping from the differences of model variables $(u_e, v_e, p_e, \theta_e, q_e)$ into differences of control variables: unbalanced pressure, streamfunction, velocity potential, non-linear humidity ($aP_e, \psi_e, \chi_e, \mu_e$ respectively) using knowledge of hydrostatic balance, geostrophic balance and the linear balance equation (Bannister, 2008b; Met Office, 2017). This is to remove any cross-covariances or correlations between $\mathbf{e}$ in different model variables. It is assumed that $\mathbf{e}$ of unbalanced and balanced variables are uncorrelated, so $\mathbf{e}$ between these control variables are uncorrelated. There are additional points to note:

- In SINGV, we still observe substantial vertical correlations between aP_e and χ_e, aP_e and μ_e in all the training data (not shown);
- Geostrophic balance is weak in the tropics, with ~85% of hydrostatic pressure forecast error variance hP_e explained by aP_e;
- The balanced component of χ_e has not been removed (predicted by regression from ψ_e), so χ_e is entirely unbalanced.

These are all important considerations but are not within the scope of this paper. To address these, it may be more appropriate in the tropics to use the model variables as control variables instead of decomposing them into balanced and unbalanced control variables (Bannister, personal communication).

For each of the $\mathbf{e}$ fields $(aP_e, \psi_e, \chi_e, \mu_e)$, the following vertical and horizontal transforms are performed. In the vertical transform, the vertical modes (eigenvectors) which best approximate all vertical columns of $\mathbf{e}$ fields in the training data must be determined (Met Office, 2013b). First, a vertical covariance matrix at each horizontal gridpoint can be computed by considering the vertical covariances between any two vertical levels. The domain-averaged vertical covariance matrix can then be computed for realisations over all horizontal gridpoints and samples. Note that the resulting vertical covariance matrix is a K by K matrix, where K is the number of model levels. This matrix can be represented by orthogonal vertical modes with no correlations between modes, weighted by their eigenvalues. Using this setup, it implies that the same set of vertical modes is used throughout the model domain, as required. The approximation of each vertical column of $\mathbf{e}$ fields is given by a linear combination of this set of vertical modes. It is useful to think of this as a projection of the vertical columns of $\mathbf{e}$ fields onto the set of vertical modes. The result is a 2-dimensional field of modal coefficients for each vertical mode which are only horizontally correlated.

In the horizontal transform, the horizontal distance-based covariances of the modal coefficient fields for each vertical mode are computed and converted to horizontal correlations. A second-order autoregression (SOAR) structure function is fit to represent the horizontal correlations, with a characteristic horizontal length-scale assigned to each vertical mode (Met Office, 2013c). This represents the horizontal correlations of each vertical mode solely as a function of distance and results in the assumption of isotropy. Also, since the same vertical modes are used with the same horizontal length-scale for the entire model domain, homogeneity is assumed.

These steps have led to a substantial reduction in the number of elements required to specify $\mathbf{B}$. It is important to note that the vertical modes and their assigned horizontal length-scales described here largely determine the horizontal and vertical structures of $\mathbf{B}$ mentioned in the paper.

ADDITIONAL REFERENCES

Met Office, VAR Technical Documentation Paper 9, 2018.

Met Office, VAR Scientific Documentation Paper 10, 2013a.

Met Office, VAR Scientific Documentation Paper 11, 2017.

Met Office, VAR Scientific Documentation Paper 13, 2013b.

Met Office, VAR Scientific Documentation Paper 14, 2013c.

The above documents are available at: https://code.metoffice.gov.uk/doc/var/var-2019.02.0/doc/,last accessed:16 July 2019

GLOSSARY

Advanced Microwave Sounding Unit (AMSU): Instrument installed on meteorological satellites that measures temperature and moisture throughout the atmosphere based on microwave radiation. The earlier unit was termed 'Microwave Sounding Unit' (MSU).

Background (data assimilation): The information retained by the NWP model from the previous cycle.

Cold surges: Strong northeasterly winds over the South China Sea that bring increased convection over the Maritime Continent during the Northeast Monsoon.

Correlation of anomalies (CORA): A measure of the linear association between predicted and observed anomalies, also termed 'anomaly correlation coefficient'. Similar to *r*, but when the variables are specifically anomalies and generally applied to a spatial field.

Data assimilation: Procedure through which observational data is used to update a NWP model.

El Niño–Southern Oscillation (ENSO): Irregular variations in the winds and sea surface temperatures over the tropical Pacific Ocean (variations in the Walker Circulation). The pattern oscillates between neutral, El Niño, and La Niña with no regular pattern.

Equatorial Rossby waves: Large planetary scale waves arising from meridional variability in the Coriolis parameter (across the equator). The waves are associated with vortices on either side of the equator and travel westwards.

Gravity waves: Waves that are generated when gravity or a buoyancy force tries to restore equilibrium when a boundary between two layers of different density fluids is disturbed.

Inhomogeneities: Non-climatic changes in a time series, for example caused by changes in sensor or location of measurement.

Intertropical Convergence Zone (ITCZ): A belt of low pressure near the equator where the trade winds from the Northern and Southern hemispheres meet, generally marked by intense convection and rainfall.

Kelvin wave: A wave that balances the Earth's Coriolis force against a boundary (e.g. a coast) or waveguide (e.g. the equator).

Madden Julian Oscillation (MJO): One of the most important and identified fluctuations in tropical weather on weekly to monthly timescales. It is often characterised as a pulse of cloud and rain that moves eastward along the equator, typically occurring every 30–60 days.

Mean square skill score (MSSS): Used for verification of deterministic forecasts. The score compares the mean square error when using the forecasts with that of the mean square error of the climatology.

Metadata: Data (or information) that describes other data (i.e. documentation of data).

Moisture flux: The rate of flow of moisture (e.g. specific humidity).

Northeast Monsoon: The boreal winter monsoon where the winds blow from the northeast over much of Southeast Asia.

Numerical Weather Prediction (NWP): Computer models that solve mathematical equations representing atmospheric physics. Used extensively in weather forecasting.

oldDS: The background error covariance matrix used as a reference for testing in MSS.

Quasi-Biennial Oscillation (QBO): A quasi-periodic oscillation of the tropical stratospheric wind (those at approximately 30km above the equator) between easterly and westerly winds. The winds oscillate with an approximate period of 28 months.

Radiosonde: The instrument carried up into the atmosphere (normally by balloon) that takes various measurements and transmits them to a ground receiver.

Re-forecasts: Similar to forecasts, but run for past dates and often uses reanalysis data as input. Re-forecasts are used in subseasonal and seasonal forecasting.

Singapore Variable Resolution (SINGV): MSS's integrated numerical weather prediction system, developed jointly in collaboration with the UK Met Office.

Structure functions (data assimilation): Mathematical functions that show how the information from observations influences other locations as it spreads out from the point of observation.

Subseasonal to seasonal (S2S) forecasts: Forecasts between the weather timescale and seasonal timescale, often considered to be forecasts for two weeks to two months into the future. Sometimes referred to as simply 'subseasonal forecasts'.

Upper Air Observatory (UAO): The observatory located in Paya Lebar from where radiosondes have been deployed since 1956.

viMF: The vertically integrated moisture flux.

Western Maritime Continent (WMC): The western part of the Maritime Continent, which includes Singapore, Peninsular Malaysia, Sumatra, as well as parts of Borneo and Java.

Website: ccrs.weather.gov.sg

Address: 36 Kim Chuan Road, Singapore